photonics

MDPI

Review

A Brief Review on Nonlinear Photonic Crystals Induced by Direct Femtosecond Laser Writing

Yaolan Tian *, Qingbo Li, Lili Yan, Xiangdong Cao and Xian Zhao

Center for Optics Research and Engineering, Shandong University, Qingdao 266237, China; zhaoxian@sdu.edu.cn (X.Z.)

* Correspondence: tianylsdu@sdu.edu.cn

Abstract: Direct femtosecond laser writing or inscription is a useful technique, and it has been employed to engineer various materials in many applications including nonlinear photonic crystals, which are of periodically patterned second-order nonlinearity to get and control the coherent light at new frequencies. By manipulation of second-order nonlinearity, either erased or poled, quasi-phase matching has been achieved in several crystals, especially three-dimensional nonlinear photonic crystals have been originally proposed and proved to be truly three-dimensional. Here we shortly review on the recent advances in the research field of nonlinear photonic crystals inscribed by femtosecond laser, as well as look into the future in this field.

Keywords: direct femtosecond laser inscription/writing; second-order nonlinearity erasing/poling; QPM; NPCs; SHG

Citation: Tian, Y.; Li, Q.; Yan, L.; Cao, X.; Zhao, X. A Brief Review on Nonlinear Photonic Crystals Induced by Direct Femtosecond Laser Writing. *Photonics* **2023**, *10*, 833. https://doi.org/10.3390/photonics10070833

Received: 24 May 2023
Revised: 1 July 2023
Accepted: 8 July 2023
Published: 18 July 2023

1. Introduction

Frequency conversion processes are employed for the generation of new, desired frequencies, which has attracted many research interests due to its existing and potential applications in nonlinear photonics, including new laser sources [1,2], nonlinear optical microscopies [3,4], optical communications [5,6], nonlinear holograms [7], optical tweezers [8–10], and quantum information [11,12]. Several processes are available to obtain nonlinear frequency conversion, including second harmonic generation (SHG), difference-frequency generation (DFG), sum-frequency generation (SFG), optical parametric oscillation (OPO), and optical parametric amplification (OPA) [13]. Among them, SHG is the most commonly used for frequency doubling. In 1962, Armstrong et al. revealed that the SHG process is dominated by phase mismatch ($\Delta\vec{k}$), which is the difference between the fundamental wave vector $\vec{k}_F$ and the second harmonic (SH) wave vector $\vec{k}_{SHG}$ [14]. Commonly, $\Delta\vec{k} \neq 0$ due to the dispersion of nonlinear crystal, and electromagnetic energy oscillates between the fundamental wave and second harmonic wave with coherent length l_C due to the dispersion of crystal. In order to obtain a good-quality and high-efficiency SH emission, phase mismatch must be eliminated.

There are generally two methods to overcome the dispersion of nonlinear crystals. One way is using birefrigent crystal, attaining birefrigence phase matching (BPM), which was first experimentally demonstrated in 1961 [15]. By choosing proper polarizations of the fundamental wave and using optical anisotropy of birefrigent crystals, the phase-matching condition is fulfilled, i.e., $\Delta\vec{k} = 0$ [13]. However, BPM is limited by the small birefrigence of some popular nonlinear crystals including $LiNbO_3$ and restricted to some specific wavelengths. Additionally, the conversion efficiency of BPM is highly limited by walk-off angle [13]. The other way is to periodically pole second-order nonlinearity ($\chi^{(2)}$) to obtain a quasiphase matching (QPM) [14–16]. Via QPM, not only can the largest nonlinear coefficient be utilized, but also can the spatial walk-off angle be avoided. As long as $\chi^{(2)}$ is spatially modulated, a reciprocal vector lattice (RVL) $\vec{G}_m$ is produced, which contributes

to interacting wave vectors [17]. Consequently, the quasiphase matching condition is $\vec{k}_F - 2\vec{k}_{SHG} - \vec{G}_m = 0$. For example, a simple 1D grating (Figure 1a) gives $G_m = \frac{2m\pi}{\Lambda}$, where m is an integer, and $\Lambda = 2l_C$ is the poling period. According to the Fourier transform, the intensity of the corresponding RVL is $\frac{2}{m\pi}$ when the duty cycle is 0.5. The first-order RVL with $m = 1$ has the largest Fourier coefficient $\frac{2}{\pi}$.

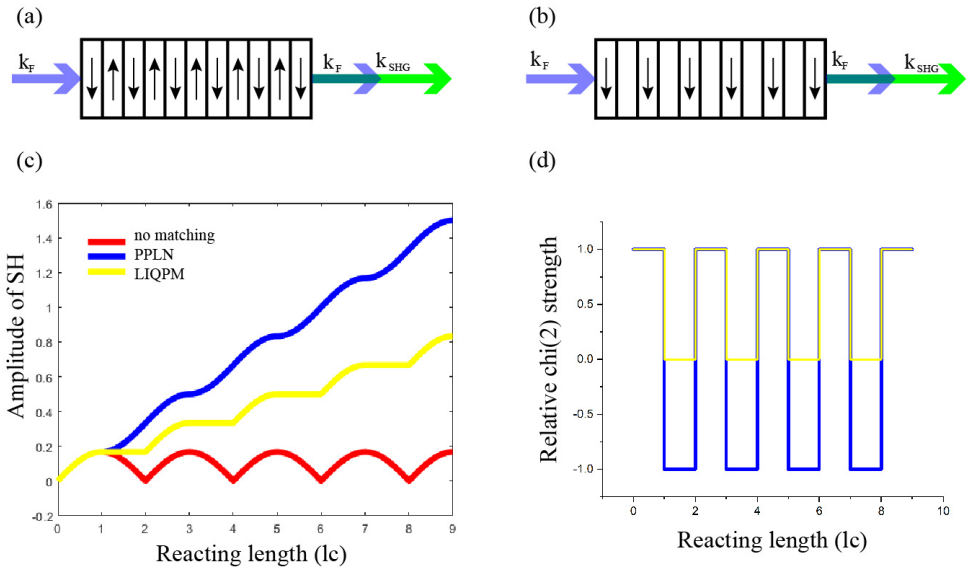

Figure 1. (**a**) $\chi^{(2)}-$poling 1D QPM and (**b**) $\chi^{(2)}-$erasing 1D QPM. In both (**a**) and (**b**), the periodicity is $\Lambda = 2l_C$ and the duty cycle is 0.5. (**c**) The amplitude of SH and (**d**) the relative $\chi^{(2)}$ value vs. the reacting length. The red line indicates the no-maching case, the blue lines indicate $\chi^{(2)}-$poling case and the yellow lines indicate $\chi^{(2)}-$erasing case.

One traditional QPM technique is to pole ferroelectric domains by electric field [18–20], and the most common method is periodically poled lithium niobate (PPLN) [21–23]. Other methods, including chemical indiffusion [24,25], crystal-growing [26], scanning force microscopic poling [27], electron-beam poling [28,29], and UV-light poling [30,31], have been developed for specific circumstances. In 1998, the 1D QPM configuration was extended to 2D and 3D by Berger, and a concept of nonlinear photonic crystal (NPC) was introduced, where $\chi^{(2)}$ is spatially periodically modulated without changing the refractive index [32]. It is analogous to photonic crystal (PC), but with a periodic controlled refractive index [33,34]. Generally, the phase-matching condition is modified as $\vec{k}_{SHG} - 2\vec{k}_F - \vec{G}_{m,n,l} = 0$, where $\vec{G}_{m,n,l}$ is a 3D RVL (Figure 2c), with n and l being integers. Correspondingly, 3D RVL is expressed as $\vec{G}_{m,n,l} = m\frac{2\pi}{\Lambda_x}\hat{x} + n\frac{2\pi}{\Lambda_y}\hat{y} + l\frac{2\pi}{\Lambda_z}\hat{z}$; Λ_x, Λ_y and Λ_z are the poling periods along the x, y and z axes respectively. So, the second harmonic emission could be versatilely generated by choosing different combinations of m, n, l, and $\Lambda_x, \Lambda_y, \Lambda_z$ [35–37].

Regarding 3D, NPCs have plenty of unique applications, such as the frequency doubling of femtosecond laser pulses [38], 3D nonlinear beam shaping [39–41], and high-dimensional entanglement [42–44]. However, the electric field required for poling in PPLN must be applied along the axis of spontaneous polarization, so these kinds of NPCs always have 1D or 2D structures [45–47]. Therefore, NPC was restricted to 1D and 2D for a long time, because no technique was able to manipulate $\chi^{(2)}$ in 3D before the direct femtosecond laser inscription of $\chi^{(2)}$ technique was developed. It is a material–light interaction, either erasing or poling $\chi^{(2)}$, introduced by a tightly focused near-infrared femtosecond laser. For the first approach, the crystalline structure of dielectric crystals is partially destroyed, resulting in a local reduction in $\chi^{(2)}$ (Figure 1b,d). The second approach is to

invert the spontaneous polarization either using a thermoelectric or a pyroelectric field. Benefiting from femtosecond laser inscription, one can manipulate $\chi^{(2)}$ in 3D inside nonlinear crystals as desired. In addition to applications in the field of photonic crystals and on-chip devices [48,49], the extension of this technique to nonlinear crystals paved the way to achieve the monolithic fabrication of 3D nonlinear integrated photonic devices for all-optical communication and on-chip signal processing. In this review, we focus on full-optical $\chi^{(2)}$-engineering techniques. We describe both the $\chi^{(2)}$-erasing and the $\chi^{(2)}$-poling techniques, demonstrating their recent progresses and applications in NPCs, and review typical femtosecond laser incription parameters.

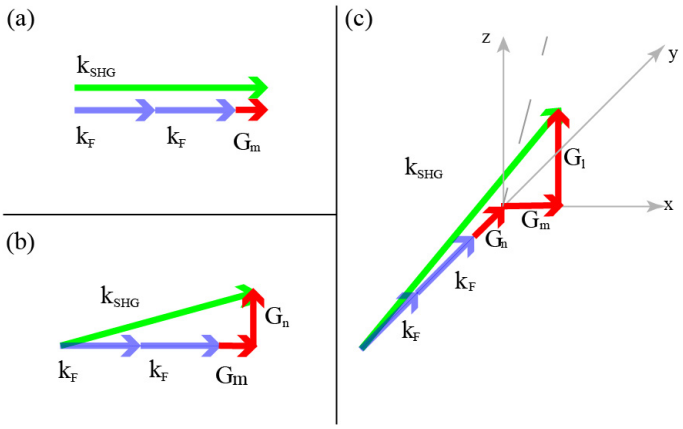

Figure 2. Schematic of the wave vectors in quasiphase matching in 1D (**a**), 2D (**b**) and 3D (**c**).

2. $\chi^{(2)}$-Erasing Technique Using Femtosecond Laser

Femtosecond laser inscription is a popular technique used to fabricate structures inside transparent materials by engineering its bulk refractive index [50]. Tightly focused pulses are nonlinearly absorbed and confined into the focal volume before excited free electrons dissipate to the surrounding area due to the short period of femtosecond pulses [51]. Multiphoton absorption [52] localized on micro and submicro scales leads to bond breaking and rebonding, constituents' migration, or thermomechanical effects [53–61]. Therefore, the refractive index is changed [62–64], which is used for many applications such as 3D optical storage [65], surface modification [66], photonic devices [67], terahertz (THz) devices [68], and optical fluid [69], especially in the field of waveguides [70–76].

Normally, two types of refractive index changes are induced [54,55,77], including the Type I modification and Type II modification. For the first type, Δn ($\Delta n>0$) is in the range of $10^{-4} - 10^{-3}$ due to a slight change or a phase transition of the crystal structure [63]. The second one refers to a large Δn ($\Delta n<0$), because that there are voids brought in by microexplosions [78]. Recently, Type I modification has been developed to engineer $\chi^{(2)}$ to achieve QPM, which is called laser-induced quasiphase matching (LiQPM). Instead of being periodically switched, $\chi^{(2)}$ is selectively erased via optimized laser engineering parameters. Generally, $\chi^{(2)}$ is partially destroyed and the residue is marked as d, defining a ratio $\nu = \frac{d}{d_{max}}$ $(0 \leq \nu \leq 1)$, where d_{max} is the crystal's second nonlinearity. $\nu = 0$ when $\chi^{(2)}$ is totally destroyed, while $\nu = 1$ when it is unchanged. The periodic erasing of $\chi^{(2)}$ also introduces a RVL, and the intensity of 1D RVL is $\frac{1-\nu}{m\pi}$ if the duty cycle is 0.5 (Figure 1b). The intensity of LiQPM is maximized as $\frac{1}{m\pi}$ when $\nu = 0$, while it is $\frac{2}{m\pi}$ for $\chi^{(2)}$-poling QPM (Figure 1a,c).

Recently, the $\chi^{(2)}$-erasing technique has attracted a lot of interests since Thomas et al. produced the first 1D LiQPM structure (Figure 3a–c) in an x-cut $LiNbO_3$ in 2013 [79]. Employing this structure, a very poor conversion efficiency of ~0.015% was observed. Imbrock et al. demonstrated a 1D grating integrated with cladding waveguides (Figure 3d–f) in a z-cut $LiNbO_3$ in 2015, which was the first demonstration of integration two types of crystal modifications induced by a femtosecond laser [80]. By reducing possible diffraction

lost, the energy conversion efficiency was increased to 5.72%. Additionally, they developed a chirped structure for broadband SHG and a cascaded single-period structure for generating parallel multiwavelength SHG [81]. In 2018, Wei et al. reported a 3D NPC by selectively erasing $\chi^{(2)}$ in a *z*-cut Mg-doped $LiNbO_3$ (Figure 4), which was the first experimental demonstration of 3D NPC using the $\chi^{(2)}$-erasing technique [82]. The conversion efficiency is considerably increased by the versatile phase-matching configuration in 3D NPC. They also proposed nonlinear beam shaping with a 3D NPC (Figure 5) fabricated via this technique [83]. Zhu et al. extended this technique to engineer $\chi^{(2)}$ on the surface of a BPM crystal and achieved high-efficiency nonlinear beam shaping [84], where the phase matching condition is fulfilled through the birefrigence in the longitudinal direction and the nonlinear Raman–Nath condition in the transverse direction (Figure 6). Furthermore, they proposed a nonlinear holography in a monolithic lithium niobite crystal [85]. Shao et al. demonstrated 1D QPM in *z*-cut quartz as well as in *x*-cut $LiNbO_3$ crystals [86]. Notably, they proposed the generation of deep-ultraviolet wave of 177.3 nm with a quartz sample with a conversion efficiency of 0.107%. They also demonstrated an angular engineering strategy of a LiQPM structure for widely tunable SHG and experimentally demonstrated it in a quartz crystal [87]. The output wavelength covered 221 to 332 nm, and the conversion efficiency at the peak power was more than 1%. Very recently, they developed a metacrystal of quartz and increased the emission conversion efficiency at 177.3/167.8 nm to 0.23%, which is close to that with RBBF [88]. Yuan et al. demonstrated a QPM structure inside a Type II waveguide in $LiNbO_3$ crystal (Figure 3g); the normalized conversion efficiency was enhanced to 8.76% $W^{-1}cm^{-2}$ [89]. Notably, the author did not point out which type of modification of the refractive index changed, but the darker line indicated a Type II modification (Figure 3g).

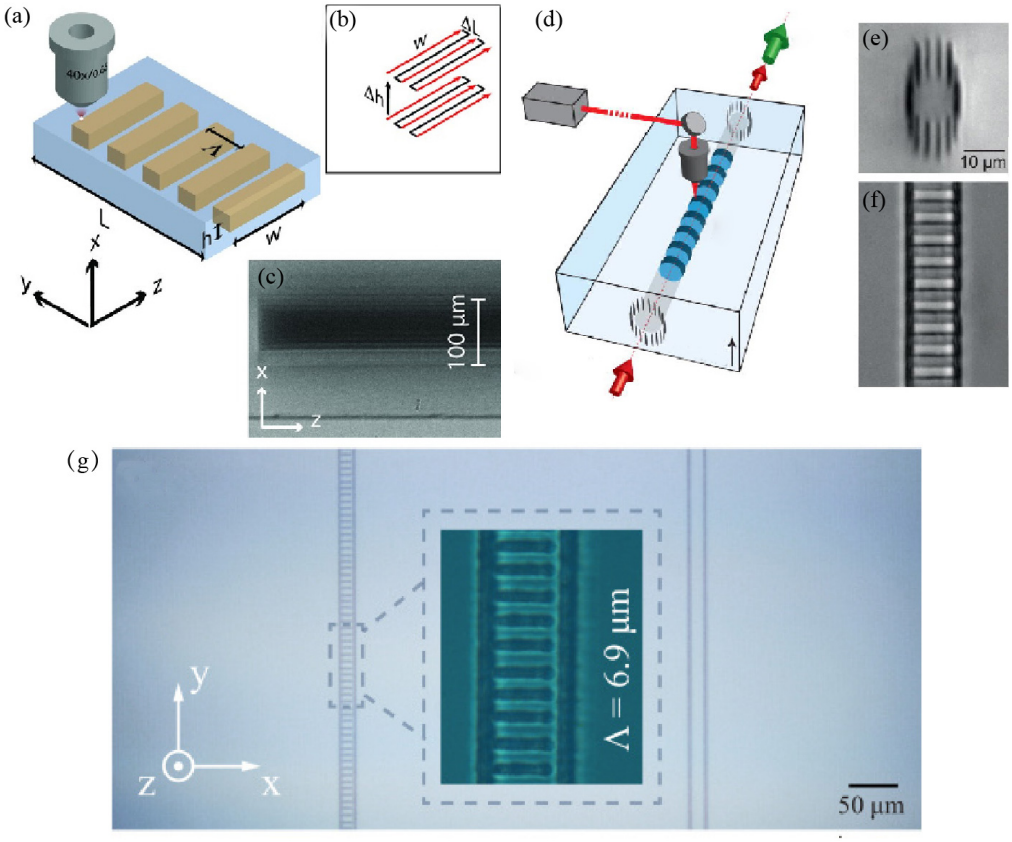

Figure 3. Three examples of LIQPM. (**a**–**c**) The first $\chi^{(2)}$-erasing grating sample. (**a**) Schematic of the sample and inscription setup, the coordinate system is principle axes of the crystal. (**b**) Each $\chi^{(2)}$-erasing

volume is complished layer by layer, and each layer is completed line by line. Shutter is on for red line and off for black line. The layers were described from surface to bottom. (**c**) An optical microscope image of a LIQPM structure. The period of the grating is 19.2 μm corresponding to a fundamental wavelength of 1545 nm. © 2013 WILEY–VCH Verlag GmbH & Co. KGaA, Weinheim; (**d**–**f**) A LIQPM grating integrated with waveguide. (**d**) Schematic of the LIQPM-waveguide design, and the grating period is 6.7 μm with a fundamental wavelength of 1064 nm. (**e**,**f**) Optical microscope images of the circular waveguide structure. The refractive index change of the cladding waveguide is TypeII modification which is relatively dark, while that of the grating is TypeI modification which is relatively bright. © 2015 AIP Publishing LIC. (**g**) Microscope image of LIQPM inside a Type II waveguide, with a period of 6.9 μm. Journal © 2023.

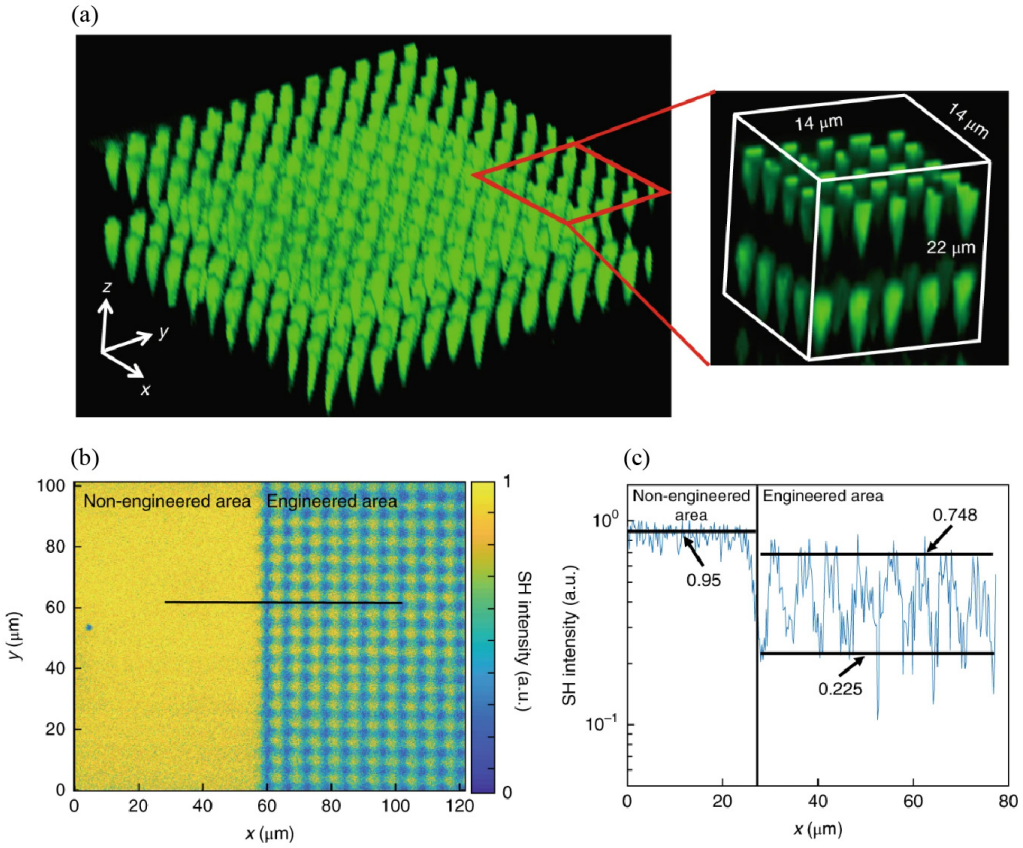

Figure 4. Characterization of 3D NPC. (**a**) A ČSHM of the first two layers of the 3D NPC, with the inserted image showing a clear periodic structure. (**b**) An image in the *xoy* plane through a general confocal SH microscopic system. (**c**) The intensity distribution along the black line in (**b**). The average values of SH intensity are also presented in (**c**) as black lines. The SH intensity is much lower in the engineered area than that in the nonengineered area, which proves the reduction in $\chi^{(2)}$ due to laser inscription. The average minimal SH intensity is 0.225, which indicates that $\chi^{(2)}$ can be further reduced. Reprinted with permission from Ref. [82], © 2018 *NaturePhotonics*.

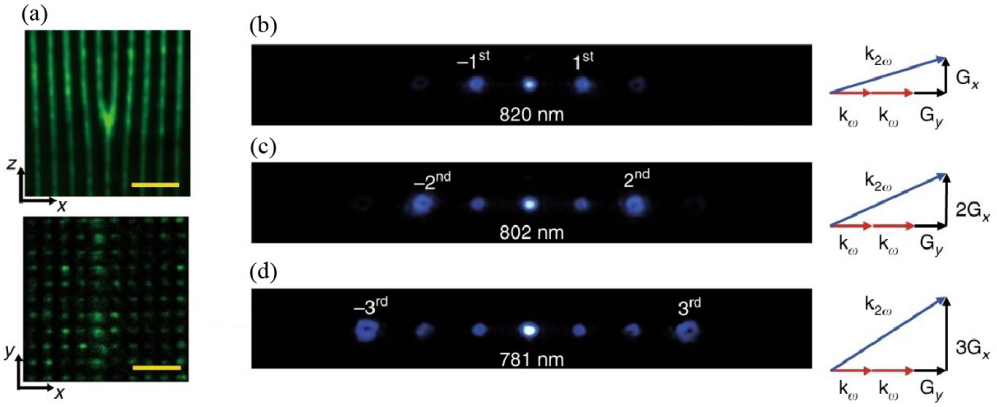

Figure 5. Far-field diffraction patterns for the 3D nonlinear fork-grating array. (**a**) ČSHM images of the 3D structures in the *xoz* plane and *xoy* plane. Here, $\Lambda_x = \Lambda_y = 3\mu m$. (**b**–**d**) SH diffraction patterns and their corresponding wave vector configurations. The 1st, 2nd, and 3rd diffraction orders are enhanced through nonlinear QPM processes at the input wavelengths of 820 nm, 802 nm and 781 nm, respectively. © 2019 Optical Society of America.

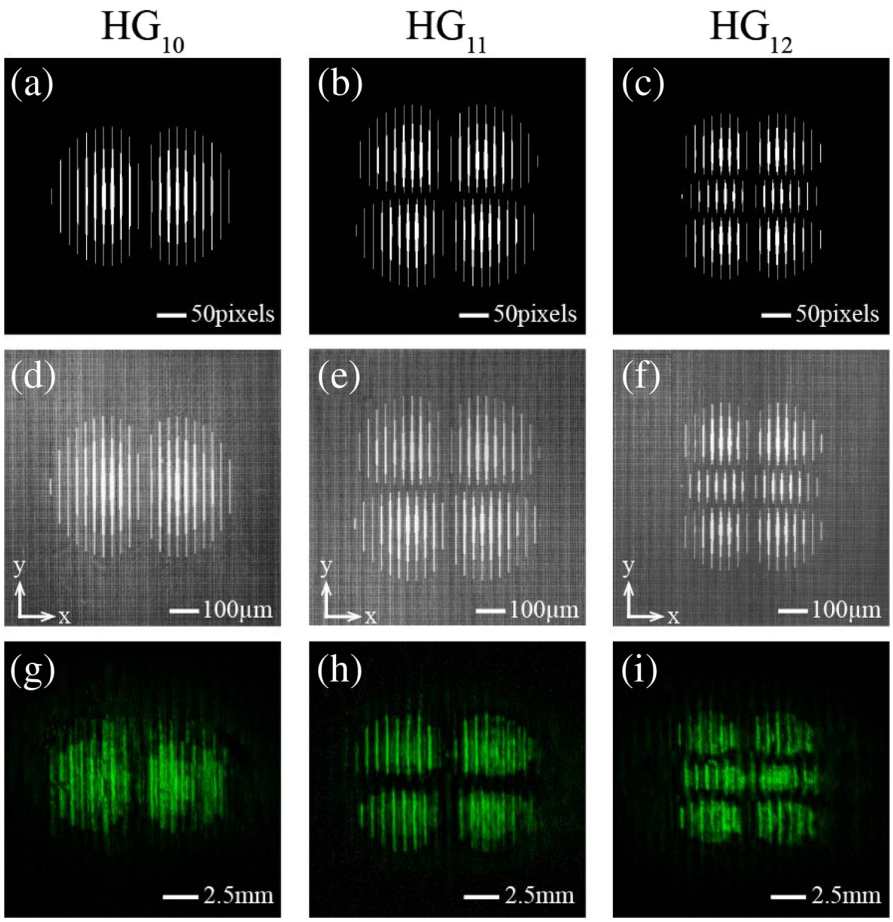

Figure 6. Comparison of the Hermite-Gaussian patterns of $HG_{(10)}$, $HG_{(11)}$, and $HG_{(12)}$. (**a**–**c**) Calculated patterns. (**d**–**f**) Optical images of the three type patterns. (**g**–**i**) ČSHM images of the three type patterns. © 2019 Optical Society of America.

3. $\chi^{(2)}$-Poling Technique by Femtosecond Laser

Laser light is employed in ferroelectric domain inversion engineering in two ways: indirectly or directly. Indirect poling of ferroelectric crystals occurs prior to the application of an external homogeneous electric field, which is enhanced by laser light to reduce the

coercive field [90–92]. Therefore, the selective uniform illumination of a femtosecond laser on ferroelectric crystal results in spatially selective domain inversion, eliminating the need for structured electrodes or crystal heating during voltage application. Several groups have reported related studies with different ferroelectric crystals using this technique [93–96]. It has been improved as a two-step voltage application under ultraviolet (UV) light either with the help of a mask [97] or a beam-writing technique [98] to realize a 2D domain inversion in MgO-doped $LiNbO_3$. Later, it was reported that UV light and an electric field do not need to be applied simultaneously [99]. However, the electric field must be applied along the polar axis of the crystal for domain inversion; consequently, the UV-assisted poling technique can never be employed in three dimensions. Direct poling with laser light was proposed in 1994 [100]. It was suggested that the strong electric field generated by the propagating ultrashort pulses could accelerate ions in the ferroelectric crystal. As a result, the kinetic energy of the ions is increased so that they are able to switch between their two stable positions, leading to spontaneous polarization flipping. Not until 2005 was it experimentally demonstrated that short ultraviolet pulses laser could promote nanoscale-domain inversions on the surface of $LiNbO_3$ crystal due to a strong absorption of UV light [101]. Later, it was discovered that the inversion of the ferroelectric domain only happens under a certain intensity of laser light, and the concept of domain reversion window was proposed [102]. It is an energy range of a continuous laser pulse that can induce domain inversion, which has been theoretically and experimentally confirmed [103]. However, there was no systematic study of the inverted structure in either Ref. [102] or Ref. [103].

Recently, several full-optical domain-inversion methods induced by femtosecond laser inscription have been approached [104–108], where the mechanisms to invert spontaneous polarization are totally different from the one proposed in Ref. [100]. Basically, ferroelectric-domain inversion is caused either by a thermoelectric field [109] or pyroelectric field [110] induced by femtosecond laser inscription or thermal annealing. Therefore, the poling mechanisms are categorized into two types: primary domain inversion due to a thermoelectric field and secondary domain inversion due to a pyroelectric field. As long as the employed femtosecond laser meets some certain requirements, $\chi^{(2)}$ is inverted instead of erased at an arbitrary place and along any orientation, with the crystalline undamaged. Consequently, $\chi^{(2)}$ is modified in such a way that there is no scattering loss; thus, the conversion efficiency is significantly increased for this type of QPM compared with that of LiQPM.

3.1. *Primary Domain Inversion*

Multiphoton absorption of a laser beam at the focal point leads to the local temperature being increased rapidly [111,112]. Consequently, the temperature gradient within the laser focal region and the surrounding area results a 3D thermoelectric field. Taking $LiNbO_3$ as an example, only the z component of this electric field is related to the domain inversion (Figure 7) [105,113], which is bipolar in the focal region: one half is antiparallel to the spontaneous polarization, while the other half is parallel to the spontaneous polarization. Additionally, ionic conductivity is increased via laser heating, leading to a local reduction in the coercive field to make it easier to invert the spontaneous polarization at the laser focal point [114]. When the thermoelectric field surpasses the coercive field, domain inversion happens in half of the focal volume, where the thermoelectric field is opposite to spontaneous polarization. In this model, the pyroelectric field is ignored within the laser focal region, because it is one order smaller than the thermoelectric field [107]. Normally, inverted domains have an elongated form due to the spherical aberration induced by refractive index differences when the laser beam enters the crystal from air [104]. The laser intensity decays along the propagating direction because its absorption is intensity-dependent. Meanwhile, the laser undergoes birefringence, which introduces multiple focuses [115,116]. Therefore, the inverted domain has a larger cross-section in the incoming direction of the laser than that in the outgoing direction [105].

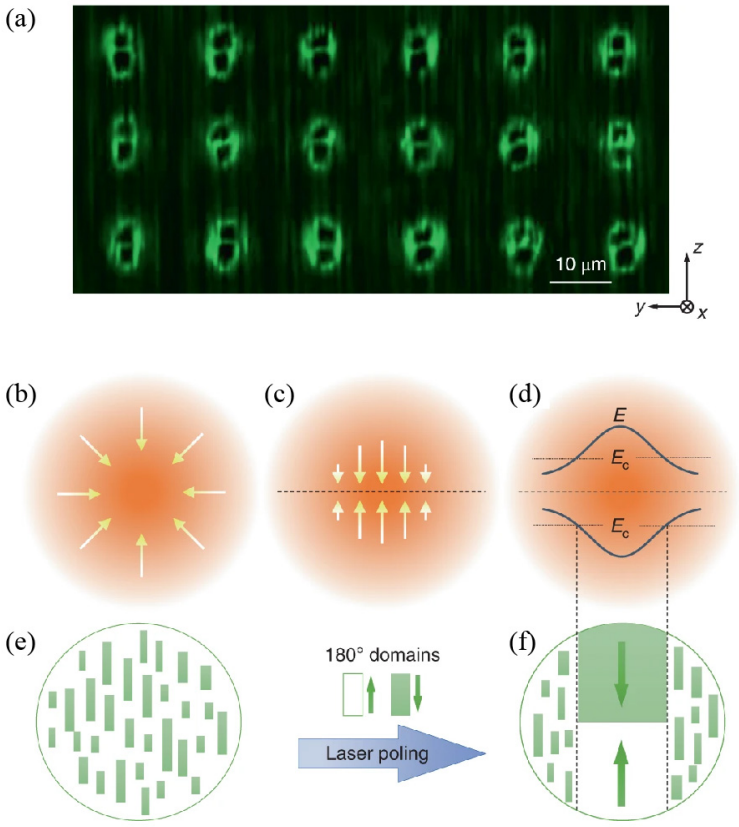

Figure 7. Ferroelectric-domain inversion induced by tightly focused femtosecond laser in the BCT crystal. (**a**) The θ -like domain structure created by femtosecond laser pulses, imaged by ČSHM. The weak random patterns surrounding the θ domain originates from random inherent submicrometre-period domains in the BCT crystal. (**b**–**f**) Mechanism of domain inversion. (**b**) Temperature gradient represented by arrows in induced by nonlinear absorption in the laser focal region acts as a thermo-electric field source. (**c**) The z component of the temperature gradient leads a bipolar electric field. (**d**) When the bipolar electricfield in (**c**) exceeds the coercive field $\mathbf{E}_C$, it inverts microdomains in (**e**) to form two larger antiparallel domains in (**f**). Reprinted with permission from Ref. [113], © 2018 *NaturePhotonics*.

The model of the primary domain inversion described above is first proposed by Sheng et al. and they have reported a series of works based on it [104,105,113]. Starting dealing with $LiNbO_3$, they demonstrated a 2D QPM structure with an engineering accuracy of about 1.5 μm [104]. Then integrating a grating structure with a waveguide, they managed to get a conversion efficiency of 17.45% for doubling a fundamental wavelength of 815 nm [105]. In contrast, the highest reported conversion efficiency via LiQPM is 5.72% [80]. Furthermore, they applied this technique to invert ferroelectric domains in a tetragonal perovskite ferroelectric crystal of barium calcium titanate (BCT) and captured a θ-like domain structure directly introduced by the 3D thermoelectric field (Figure 7). It is clear that there is a central horizontal line representing the domain wall, perpendicular to the spontaneous polarization of the BCT. Furthermore, they demonstrated a 3D photonic crystal of simple tetragon fabricated using this technique and obtained two types of SHG: a square lattice of SH spots located at the center, which was standard nonlinear Raman–Nath diffraction [35]; and peripheral spots distributed as homocentric rings situated relatively far from the center, which provided direct evidence of the 3D characteristics of the nonlinear interaction.

They keep studying on this topic and reported several applications of nonlinear beam shaping employing calcium barium niobate (CBN) crystals. Firstly, they demonstrated an experiment of nonlinear wavefront shaping through a 3D NPC [117]. In this report, the 3D nonlinear structure of three layers including a fork and linear and circular gratings was proposed and employed for parallel 3D nonlinear wave shaping. Those three patterns were transversely overlapped inside a CBN crystal and simultaneously converted a fundamental Gaussian beam into three pairs of second-harmonic vortices, Gaussians, and conical beams. In addition, the 3D nonlinear wavefront shaping was dynamically controlled for the first time by adjusting the distance between two adjacent patterns. Secondly, they promoted a curved fork pattern (Figure 8) to approach a perfect vortex second harmonic, of which the diameter was insensitive to the topological charge [118]. This was the first demonstration of perfect vortices via the nonlinear beam-shaping method, which has been realized in linear optics [119,120]. Thirdly, they studied a real 3D nonlinear volume hologram of high quality [121], where a vortex second harmonic with zero-intensity in the center was generated effectively at the resonance frequency. Fourthly, they also achieved 2D and 3D NPCs of hexagonal patterns in single ferroelectric-domain CBN crystals [122]. In this work, multiple-ferroelectric-domain CBNs were made into single-ferroelectric-domain crystals before patterns were inscribed. Subsequently, those samples were used in an SHG experiment via nonlinear Raman–Nath diffraction, and they obtained a similar SHG pattern, as shown in Ref. [113]. The generated second-harmonic emission possessed hexagonal symmetry, with its intensity increasing monotonically along the propagation. Comparing those SH emissions via 3D NPC and 2D NPC, the one generated via 3D PNC was much higher, as expected. In addition, the 2D NPC pattern was also produced in a multidomain CBN crystal, and the SH emission via the single-domain sample was higher. The poled domains appeared to be stable and can be completely erased by thermal annealing above the Curie temperature for 30 min, as were the single-ferroelectric domain.

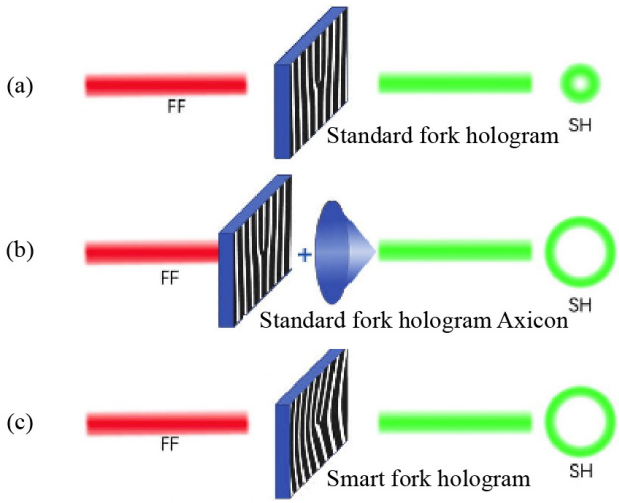

Figure 8. Schematic of evolution of nonlinear hologram of NPC. (**a**) A fork pattern leads to a second-harmonic emission of a standard optical vortex. (**b**) The fork pattern in (**a**) combined with an external axicon results in the formation of a perfect vortex harmonic. (**c**) A curved fork pattern instead of the combination in (**b**) also leads to a perfect vortex second harmonic. © 2020 Author(s).

A second model of primary domain inversion was proposed by Xu et al. [107]. They demonstrated a nonreciprocal femtosecond-laser-writing technique in $LiNbO_3$ with a resolution of 30 nm, where the 3D domain inversion is rewritable. Noticeably, a prefabricated drain is required in this model to effectively guide the electric charges produced during the poling process, without which the laser inscription of the same parameters can never produce an inversion of the domain. This engineering process can be properly simulated,

assuming that the input laser has an intensity of Gaussian profile. Thus, it could be expressed as: $I = I_0 G(x, y, x)$, where I_0 is a constant current, and $G(x, y, z)$ is a 3D Gaussian function. Since $LiNbO_3$ crystal has strong absorption at 318 nm and the wavelength of the femtosecond laser utilized here is 800 nm, the nonlinear absorption is a three-photon process [111,112]. Thus, the generated heat is

$$Q = \gamma I^3, \tag{1}$$

where γ is the three-photon absorption coefficient of $LiNbO_3$. Now, a solid heat-transfer model is considered as follows:

$$\rho C_p \nabla T \mathbf{u} - \kappa \nabla^2 T = Q, \tag{2}$$

where ρ is the density, C_p is the heat capacity, and κ is the thermal conductivity of $LiNbO_3$ crystal. T is the temperature, and $\mathbf{u}$ is the velocity vector. Suppose S is the Seebeck coefficient, the temperature gradient between the hot laser focal point and the cold surrounding area induces an electric field:

$$\mathbf{E} = S\Delta T. \tag{3}$$

The simulated 3D thermoelectric field $\mathbf{E}$ is shown in Figure 9a, and its z components are presented in Figure 9c, with $\mathbf{E}_1$ parallel and $\mathbf{E}_2$ antiparallel to the spontaneous polarization. Within the enclosed ellipsoidal area denoted by a and b, the thermoelectric field exceeds and flips the spontaneous polarization when antiparallel to it. For example, in Figure 9c, only $\mathbf{E}_2$ flips the local spontaneous polarization. Therefore, this poling technique strongly depends on the laser-writing direction and is rewritable. As shown in Figure 9d, the laser both comes and writes along the $+z$ direction, which is also the spontaneous polarization direction. Figure 9d,g indicate that when the laser beam moves along the $+z$ direction, $\mathbf{E}_2$ switches the polarization back regardless of the direction. If it is flipped, the laser acts as an eraser; if it is normal, the laser does not work at all. In the contrast, when the laser moves along the $-z$ direction, $\mathbf{E}_1$ overtakes $\mathbf{E}_2$, and the domain is inverted (Figure 9e) with a width of a. In another case, as shown in Figure 9f, the laser moves along the y axis of the crystal and half of the laser focal area is inverted by $\mathbf{E}_1$ with a width of b. Therefore, with a proper design, a focused laser beam can be used as a laser pen or eraser to fabricate arbitrary 3D ferroelectric-domain structures.

A third model following the same principle with the primary domain inversion was developed by Wang et al. [108]. It is a two-step poling technique: in the first step, laser marking, a tiny seed is created by a single pulse illuminated along the z-axis either on the surface or inside the $LiNbO_3$ crystal, shorted for LM; in the second step, laser inducing, a temperature gradient is induced by moving the focal point of the multiple laser pulses away from the seed, shortened as LI. This high temperature gradient induces a 3D thermoelectric field, which not only makes the domain inverted but also drives inverted domain growth when it surpasses the coercive field. LMs, which are Type II modifications, can be inscribed not only on the surface but also inside the crystal, requiring different pulse energies to compensate for the slight loss during propagation. Generally, the seeds have uncontrollable, random quality. Therefore, oversized or downsized seeds make it harder to pole the ferroelectric domains; unfortunately, this mechanism is not understood yet. Furthermore, because the coercive field varies at each point of the crystal, correspondingly, the minimum energy of the multiple laser pulses for inducing the poling varies from 600 nJ to 700 nJ. It must be mentioned that a single LI can simultaneously invert ferroelectric domains along thousands of seeds within a region of about 200 µm; thus, this method is highly efficient and energy-saving.

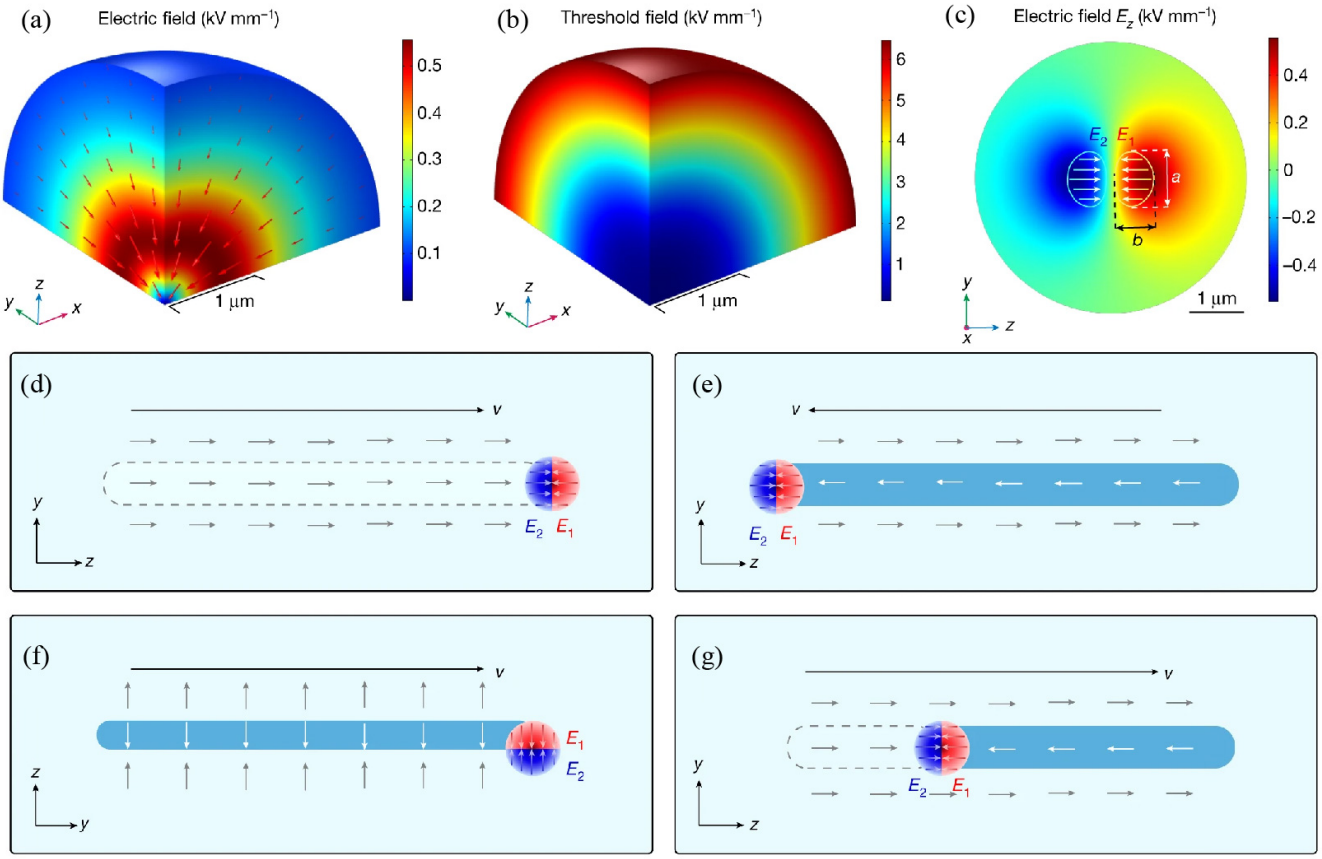

Figure 9. The working principle of non-reciprocal laser writing for $LiNbO_3$ ferroelectric-domain engineering. (**a**–**c**) The simulated electric field. (**a**) The 3D thermoelectric field induced by the temperature gradient. (**b**) The threshold of $LiNbO_3$ for domain inversion, whose magnitude depends on local temperature. (**c**) The z components of the thermoelectric field. Within the enclosed ellipsoidal areas, these are denoted by a and b. The z components $\mathbf{E}_1$ and $\mathbf{E}_2$ of the thermoelectric fields are higher than the threshold field. Only the one antiparallel to the spontaneous polarization of $LiNbO_3$ can pole the domain. (**d**–**g**) The principle of the nonreciprocal laser poling and erasure in $LiNbO_3$, which strongly depends on the applied sequence of $\mathbf{E}_1$ and $\mathbf{E}_2$. (**d**) Firstly, $\mathbf{E}_1$ poles the ferroelectric domains; subsequently, $\mathbf{E}_2$ inverts the domain inverted by $\mathbf{E}_1$, resulting in no inversion of the domain at the end. (**e**) When laser is moving along the $-z$ axis, $\mathbf{E}_2$ does not work, but $\mathbf{E}_1$ works to invert the domain. (**f**) When the laser scans along y axis, $\mathbf{E}_1$ and $\mathbf{E}_2$ separately interact with the spontaneous polarization, leading to an inverted domain of width b. (**g**) Supposing that the domain is inverted at the beginning, it is flipped back by scanning laser along $+z$ axis. Reprinted with permission from Ref. [107], © 2022.

3.2. *Secondary Domain Inversion*

The model of secondary domain inversion is also a two-step process: laser inscription and ten heat annealing, which is similar with the one demonstrated in previous reports. Laser-induced filaments act as seeds to induce domain inversion in subsequent thermal treatment, which was first demonstrated by Imbrock et al. [106].

A pyroelectric field instead of a thermoelectric field plays an important role here. More specifically, the sum of the depolarizating field $\mathbf{E}_{dep}$ due to the spontaneous polarization, screening field $\mathbf{E}_{scr}$, and thermally activated bulk charges is taken into account to explain the mechanism of domain inversion. In some certain ferroelectric crystals such as $LiNbO_3$, domain back switching and domain wall motion can be promoted by a ,temperature change. Heating or cooling temporarily changes the magnitude of spontaneous polarization;

therefore $\mathbf{E}_{dep}$ is temperature-dependent. Normally, the pyroelectric field $\mathbf{E}_{pyr}$ can be expressed as:

$$\mathbf{E}_{pyr} = \mathbf{E}_{dep} + \mathbf{E}_{scr}. \quad (4)$$

At room temperature, $\mathbf{E}_{dep}$ is fully screened by bulk and surface charges; thus, $\mathbf{E}_{pyr} = 0$ (see Figure 10a). When the crystal is being heated, the polarization decreases, leading to a reduction in $\mathbf{E}_{dep}$. Therefore, $\mathbf{E}_{pyr}$ is not zero any more, and the net value is parallel with $\mathbf{E}_{scr}$ (Figure 10b), which can be expressed as:

$$\mathbf{E}_{pyr} = -\frac{1}{\epsilon\epsilon_0}(p)\Delta T, \quad (5)$$

where ΔT is the temperature change, and p is the pyroelectric coefficient. Meanwhile, thermal heating activates charges to drift into the pyroelectric field, resulting a new field of charges $\mathbf{E}_{cha}$ parallel to $\mathbf{E}_{dep}$ to compensate for $\mathbf{E}_{pyr}$ (Figure 10c). Now, the pyroelectric field is zero again and expressed as

$$\mathbf{E}_{pyr} = \mathbf{E}_{dep} + \mathbf{E}_{scr} + \mathbf{E}_{cha} \quad (6)$$

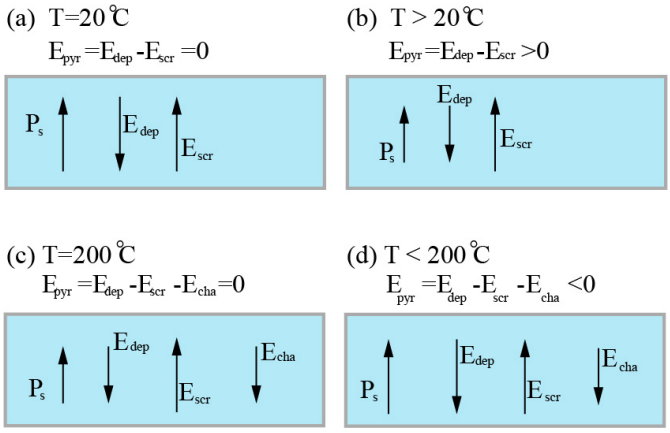

Figure 10. The pyroelectric field changes with temperature. (**a**) The pyroelectric field is zero at room temperature. (**b**) It is not zero any more and parallel to the spontaneous polarization ($\mathbf{P}_s$) during heating, with $\mathbf{E}_{dep}$ decreasing as temperature increases. (**c**) It is zero again at 200 °C due to the electric field induced by charges. (**d**) It is antiparallel to $\mathbf{P}_s$ when cooling down to room temperature. During cooling, $\mathbf{E}_{dep}$ increases, and $\mathbf{E}_{pyr}$ is opposite to $\mathbf{P}_s$; then, the polarization is flipped when $\mathbf{E}_{pyro} > \mathbf{E}_{threshold}$.

The concentration of the charges is higher inside the filament than that in the unexposed area, which leads to a larger charge field and a larger domain inside the filament [123]. Subsequently, the spontaneous polarization increases, and the $\mathbf{E}_{dep}$ enlarges as well in the process of cooling down, resulting in a pyroelectric field antiparallel to $\mathbf{E}_{scr}$ (Figure 10d). When the value of this pyroelectric field in the exposed area is larger than the threshold electric field, the spontaneous polarization is inverted.

This technique is suitable for ferroelectric crystals with high pyroelectric coefficients, and one of them is $LiNbO_3$, which has a dielectric as large as 28 and a pyroelectric coefficient $p = -0.38 \times 10^{-4}$ C/(m^{2}K) [124]. A unidirectional domain inversion along the z axis of MgO-doped lithium niobate crystal was proposed in Ref. [106] (Figure 11). Filaments locate either on the surface or in the middle of the z axis, and the corresponding domain inversions are extended either to the other surface or to both sides. The width of the domain inversion depends on the fluence of the femtosecond laser and the length of the filament. Moreover, the domain can have a high aspect length/width ratio of up to 800 µm/1 µm with all domain boundaries being straight over the entire domain length. Furthermore, the effect of temperature during the heating treatment and the lattice periods on the number and size of inverted domains were investigated in a 2D NPC [123]. A threshold temperature

was identified as 190 °C, and an optimal temperature regime was 220–300 °C, within which all domains could be inverted in a 2D rectangular lattice with periods of 15 μm × 6.3 μm. Above 300 °C, the already inverted domains switched back. Smaller lattice periods and lower temperatures resulted in fewer inverted domains, while the average of the central domains was 2.38 μm, which was almost independent of the temperature and lattice periods. In addition, the normalized effective nonlinear coefficients $|G_{10}|^2$ of the 2D NPC under study were calculated in the order of 1%. This limitation is due to the small duty cycle restricted by this method.

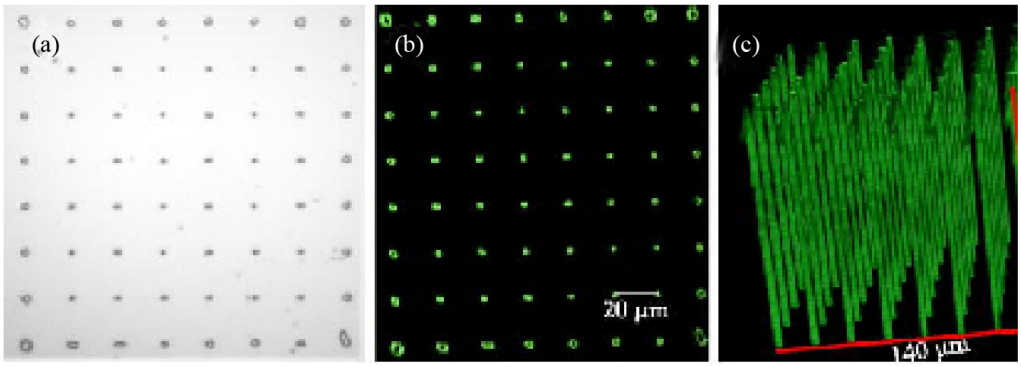

Figure 11. Square lattic pattern with a period of 20 μm. (**a**) Microscopy image of the lower surface of the crystal after selective chemical etching. (**b**) ČSHM image of the same plane as in (**a**). (**c**) The structure in the volume of the crystal measured in 3D with ČSHM. © 2018 Author(s).

3.3. Two Types of Domain Inversion Simultaneously Occurring

PT-relaxor ferroelectrics not only exhibit excellent piezoelectric but also show large second-order nonlinearity; therefore, they are good candidates for NPCs. One of them is 0.62 Pb $(Mg_{1/3}Nb_{2/3})O_3$-0.38 $PbTiO_3$ (PMN-38PT), which is a single-domain crystal and has a coercive field of 8.25 kV cm $^{-1}$ [125]. As a comparison, the coercive field for intrinsic $LiNbO_3$ crystal is about 5420 kV cm^{-1} and, for the congruent $LiNbO_3$ crystal, it is 210 kV cm^{-1} [126,127]. Therefore, domain inversion is relatively easier to attain in PMN-38PT crystal than in $LiNbO_3$. Recently, primary and secondary domain inversions were simultaneously achieved in PMN-38PT crystal by Sheng et al. [128]. The nonlinear absorption of a femtosecond laser not only leads to a thermoelectric field, inducing a primary domain inversion at the focal region, but also generates free carriers inside it, leading to a secondary domain inversion around it (Figure 12c), depending on the laser beam power. Here, the secondary domain inversion is based on the same mechanism as proposed in Ref. [106], which as described in the previous subsection. However, there are two significant differences: it has a hollow cylindrical structure (Figure 12) and grows only on one side of the focus. This is because that the redistribution of the free carriers results in a cylindrically symmetric space charge field; the pyroelectric field is unidirectional outside the focal region, while the thermoelectric field is bipolar inside the laser focal region. Furthermore, the laser has an effect of erasure on the secondary domain inversion. The thermoelectric field can switch back the flipped spontaneous polarization induced by the pyroelectric field in the overlapping area when the interval distance between two patterns is small enough (Figure 12e,f). This mechanism is similar to that described in Ref. [107]. Sheng et al. also developed a 1D QPM structure and firstly demonstrated a quasiphase matched collinear SHG in PMN-38PT crystal [129]. Three different processes of nonlinear interaction were observed by controlling the linear polarization of the fundamental beam. In addition, the relative strength of all second-order nonlinearity tensor elements were determined by comparing the emission power of the SHG at QPM resonances, and the absolute value of the d_{31} was computed as 1.3 pm/V, which was the first quantitative measurement of nonlinear properties of a PMN-38PT crystal.

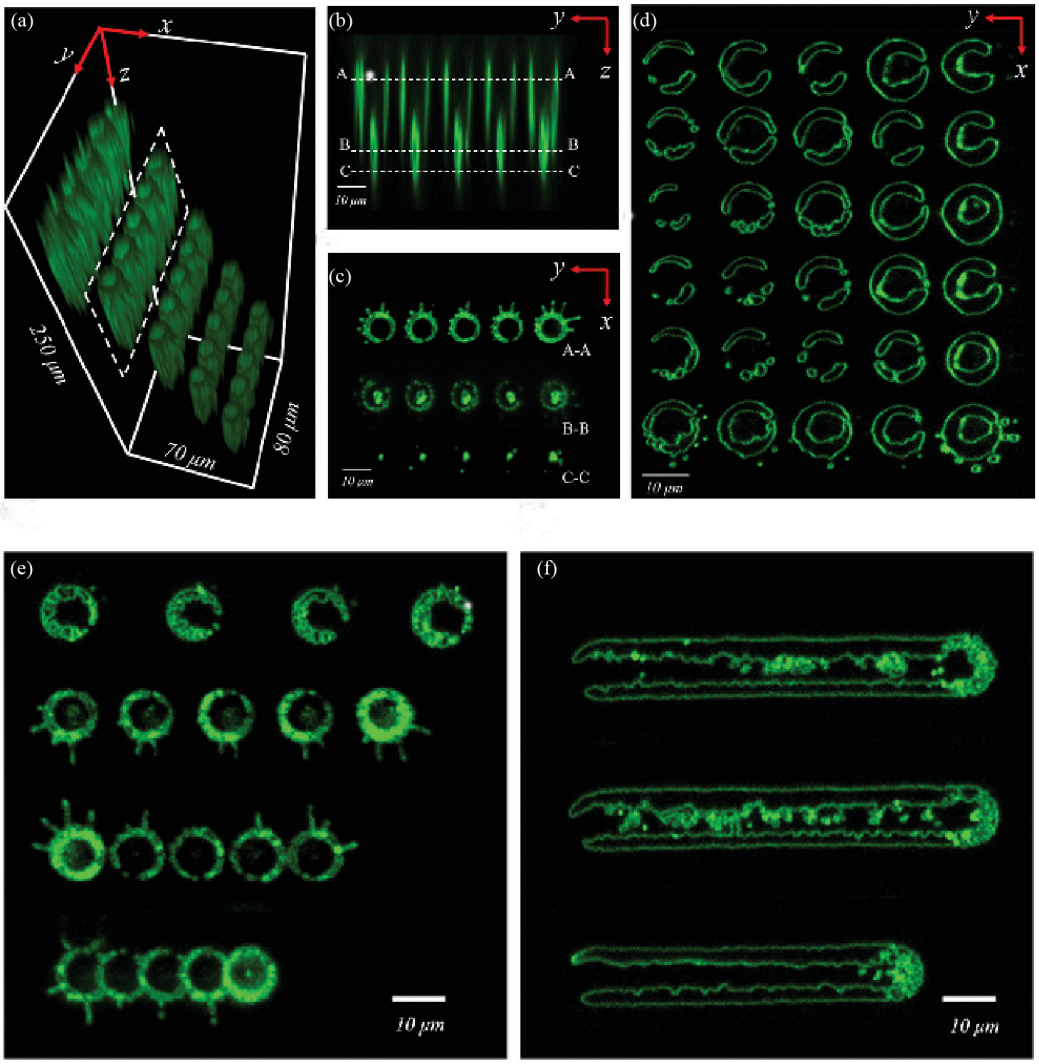

Figure 12. ČSHM images of the primary and secondary ferroelectric domains in PMN-38PT. (**a**) Laser-induced domains located at different depths inside a single-domain PMN-38PT crystal. (**b**) The view of the *yoz* cross-section corresponding to the single row bounded by the dashed line in (**a**). (**c**) The view of the *xoy* cross-section corresponding to the dashed lines in (**b**); C-C shows only primary domain inversion, B-B presents both primary domain inversion in the center and secondary domain inversion in the surrounding area, and A-A shows only secondary domain inversion. (**d**) Another example of secondary domain pattern. (**e**,**f**) Erasure of secondary domains by laser inside PMN-38PT. (**e**) Secondary domain formed with separation distance $\Lambda = 45, 15, 11, 8$ μm. (**f**) Linear secondary domain patterns formed with separation distance $\Lambda = 2$ μm for the top two patterns and $\Lambda = 1$ μm for the bottom one. © 2021 Wiley-VCH GmbH.

4. Laser Writing Parameters

For both the $\chi^{(2)}$-erasing or $\chi^{(2)}$-poling techniques, the laser-writing parameters including pulse energy and scanning speed strongly depend on the properties of the applied crystals and specific structures. Generally, mode-locked Ti:Sapphire femtosecond laser systems with regenerative amplifiers are employed as light sources due to their stabilities. Normally, the centered wavelength is 800 nm, the FWHM ranges from 75 fs to 180 fs [104,106,107], and the applied pulse energy of the laser is significantly dependent on the application purpose of the laser beam. Some typically detailed inscription parameters are listed in Table 1.

Table 1. Selected laser-writing parameters.

$\chi^{(2)}$-Erasing	Reference	Nonlinear Crystal	Repeat Frequency	Bandwidth	Wavelength	Pulse Energy	Scan Speed	N.A.
	Ref. [79]	$LiNbO_3$	100 kHz	170 fs	800 nm	650 nJ	1 mm/s	0.5
	Ref. [80]	$LiNbO_3$	1 kHz	120 fs	800 nm	60–72 nJ	80 μm/s	0.8
	Ref. [82]	$LiNbO_3$	1 kHz	104 fs	800 nm	100–200 nJ	55–100 μm/s	0.8
	Ref. [84]	MgO-doped $LiNbO_3$	1 kHz	500 fs	1030 nm	900 nJ	280 μm/s	0.5
	Ref. [86]	$LiNbO_3$ Quartz	200 kHz	350 fs	1040 nm	16/20 nJ 8/12 nJ	1 mm/s	0.3
$\chi^{(2)}$-Poling	References	Nonlinear Crystal	Repeat Frequency	Bandwidth	Wavelength	Pulse Energy	Scan Speed	N.A.
	Ref. [104]	$LiNbO_3$	76 MHz	180 fs	800 nm	0–5 nJ	10 μm/s	0.65
	Ref. [113]	BCT	76 MHz	180 fs	800 nm	∽6 nJ	10 μm/s	0.65
	Ref. [117]	CBN	76 MHz	180 fs	800 nm	3.6–6.6 nJ	10 μm/s	0.65
	Ref. [128]	PMN-38PT	80 MHz	180 fs	800 nm	0–5 nJ		0.4
Seeds	Ref. [106]	MgO-doped $LiNbO_3$	1 kHz	100 fs	800 nm	50–500 nJ		0.8
LM LI	Ref. [108]	MgO-doped $LiNbO_3$	1000 kHz 500 kHz	170 fs	1026 nm	150 nJ 300–900 nJ		0.42

More specifically, for the $\chi^{(2)}$-erasing progress, small structures with a cross-section of several tens of micrometers in diameter have been inscribed by low repeat frequency of 1 kHz with scan speeds varying from 50 to 100 μm/s (Figure 3f,g) [80,82]. Pulse energy here varies from 100 nJ to 200 nJ depending on the depth and specific crystal. Large-scale patterns with a cross-section of several hundreds of micrometers in diameter were fabricated with a medium repeat frequency of a hundred kilohertzs, scan speed of 1 mm/s, and single pulse energy as large as 650 nJ (Figure 3c) [79]. Additionally, compact ytterbium-doped diode-pumped ultrafast amplified lasers were also employed as light sources; a laser with an FWHM as large as 500 fs and a wavelength of 1030 nm was used to erase $\chi^{(2)}$ [84]. In this report, the repeat frequency was 1 kHz with a scan speed of 280 μm/s, and the single-pulse energy was 900 nJ.

Generally, pulse energy used for directly inducing poling of $\chi^{(2)}$ is smaller than that used in LIQPM, because the crystal structure must not be destroyed in this case. For example, in Ref. [104], the repeat frequency employed was around 76 MHz and the corresponding pulse energy was no larger than 5 nJ, which was optimized by depth. Generally, the scan velocity is as slow as 10 μm/s, which is time-consuming. Notably, in both the two-step primary domain inversion [107,108] and two-step secondary domain inversion techniques [106,123], the first-step seed inscribed by a femtosecond laser is a Type II modification on the crystal. In this step, the pule energy, period distance, or after-heating temperature could be factors affecting the sizes of the inverted domains in the next step. For example, in Ref. [106], seeds were induced with a repetition rate of 1 kHz with energies from 50 to 550 nJ; the inverted domain width roughly increased with pulse energy (Figure 13). It was also demonstrated that annealing temperature does not seem to affect domain size (Figure 14) [123].

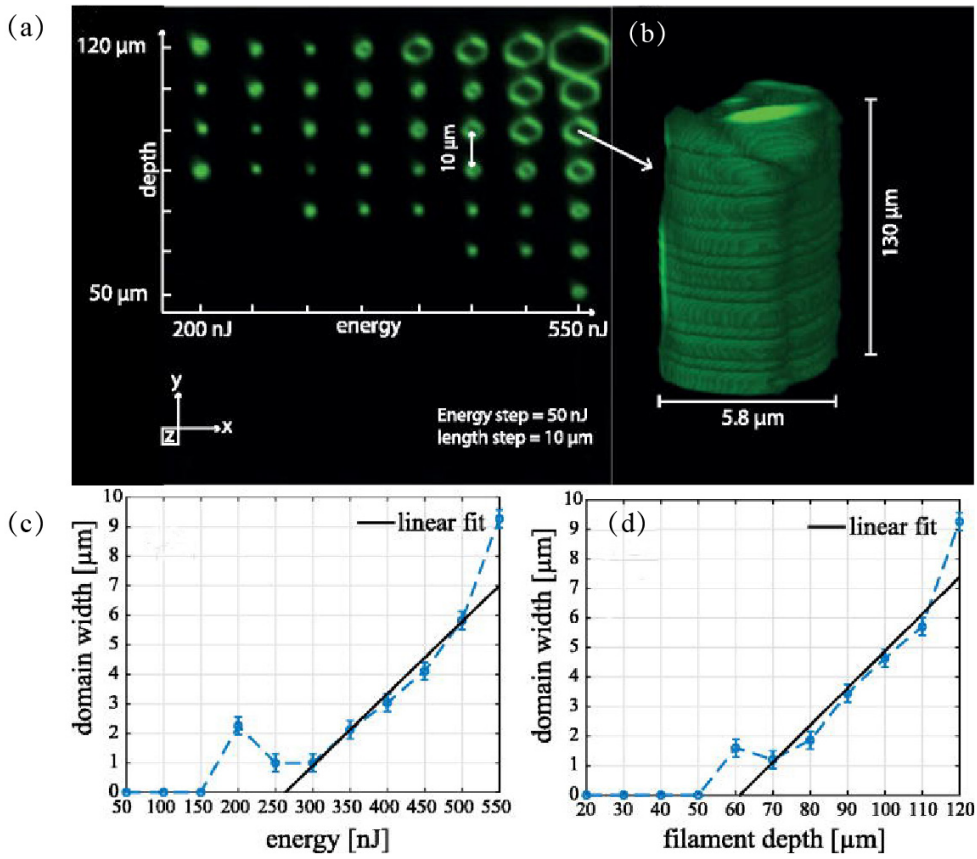

Figure 13. (**a**) ČSHM images of domains in *xoy* plane for pulse energies from 220 nJ to 550 nJ, and addressed depths of the laser-induced filaments. (**b**) The single domain marked with an arrow is shown in detail. Width of domain in (**a**) as a function either of pulse energy (**c**) or of addressed filament depth (**d**). © 2022 Author(s).

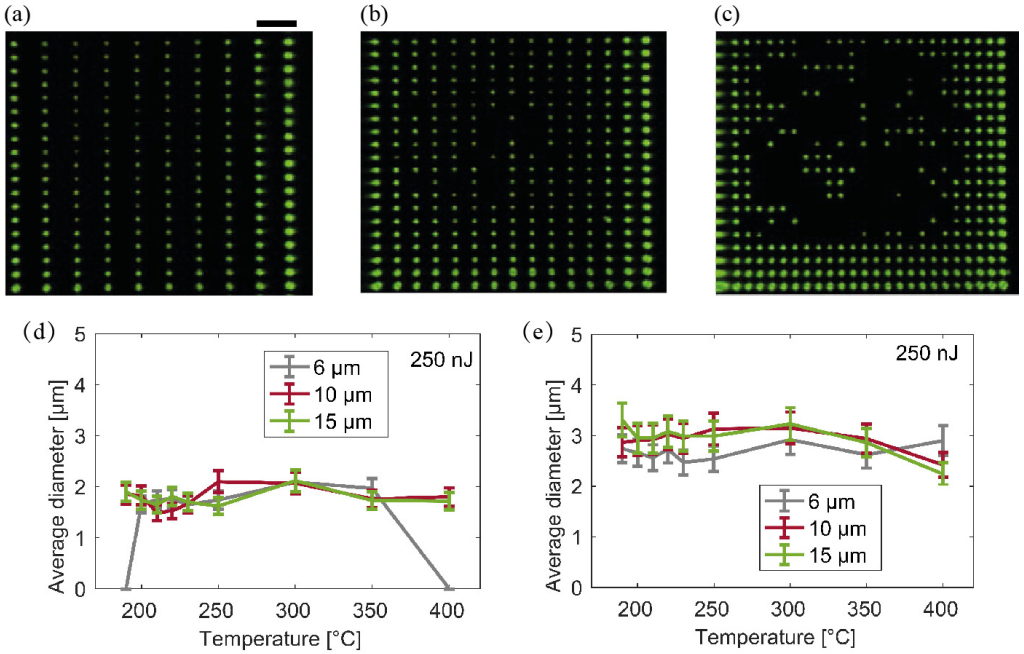

Figure 14. Average domain diameter dependent on the set temperature in a secondary domain inversion with pulse energy of 250 nJ. (**a**–**c**) ČSHM images of domains at the bottom +*z*-surface. Λ_y keeps 6.3 μm all three figures, while Λ_x = 15 μm in (**a**), Λ_x=10 μm in (**b**), and Λ_x=6 μm in (**c**). The average domain diameter of either edge domains (**d**) or in the center of lattice (**d**) dependent on the maximum heating temperature. Journal © 2022.

5. Conclusions

In conclusion, recent advances and achievements in the field quasiphase matching structures using direct femtosecond laser writing techniques were briefly overviewed. This review first briefly introduced the concept of nonlinear photonic crystal and then focused on the quasiphase matching structures achieved by full-optical methods, either erasing or poling $\chi^{(2)}$, which produce efficient SH emission. Direct femtosecond laser writing on $\chi^{(2)}$ has enormous potential owing to its unique 3D microfabrication ability, which is unmatched by other methods. Moreover, 3D QPM technology has been showing great advantages and will play a significant role in the field of nonlinear photonics, providing a promising technique for versatile integrated optical applications including frequency conversion, nonlinear Talbot imaging [130], on-chip entangled light sources [42,43], THz devices [68], 3D nonlinear holography, and beam shaping [83,84]. Nevertheless, there are some challenges to be further overcome; for example, the quality of the emission needs to be improved, as does the conversion efficiency. Additionally, it is necessary to investigate the affects of related parameters. Overall, full-optical engineering on $\chi^{(2)}$, especially the $\chi^{(2)}$-poling technique, is just starting application in 3D NPCs; its multifunctional applications in integrated on-chip photonics need to be explored in the future.

Author Contributions: Writing—original draft preparation, Y.T.; writing—review and editing, Y.T., Q.L., L.Y., X.C. and X.Z. All authors have read and agreed to the published version of the manuscript.

Funding: This research received no external funding.

Institutional Review Board Statement: Not applicable.

Informed Consent Statement: Not applicable.

Acknowledgments: Thanks for all the colleagues in Center for Optics Research who help me a lot on the way of scientific research. Especially thanks my collaborative mentor Xian Zhao, who gives me a lot help both in work and life.

Conflicts of Interest: The authors declare no conflict to interest.

Abbreviations

The following abbreviations are used in this manuscript:

1D	One-dimensional
2D	Two-dimensional
3D	Three-dimensional
SHG	Secpnd harmonic generation
DFG	Difference-frequency generation
SFG	Sum-frequency generation
OPO	Optical parametric generation
SH	Second harmonic
BPM	Birefringence Phase Matching
QPM	Quasi-phase matching
RVL	reciprocal vector
PPLN	Periodically poled lithium noibate
NPC	Nonlinear photonic crystal
PC	Photonic crystal
UV	Ultraviolet
ČSHM	Čerenkov SH microscopy

References

1. Wu, A.; Xu, J.; Zheng, Y.; Liang, X. Crystal growth and application of large size YCOB crystal for high power laser. *Opt. Mater.* **2014**, *36*, 2000–2003. [CrossRef]
2. Li, Y.; Huang, X.; Mao, W.; Xu, J.; Duan, Y.; Zhu, H. Compact 589 nm yellow source generated by frequency-doubling of passively Q-switched Nd:YVO_4 Ramen laser. *Microw. Opt. Technol. Lett.* **2023**, *65*, 1122. [CrossRef]
3. Mazumder, N.; Balla, N.K.; Zhuo, G.; Kistenev, Y.V.; Kumar, R.; Kao, F.; Brasselet, S.; Nikolaev, V.V.; Krivova, N.A. Label-free nonlinear multimodal optical microscopy–basics, development, and applications. *Front. Phys.* **2019**, *7*, 170. [CrossRef]
4. Zheng, Z.; Zhou, N.; Zhou, R. Enhancing Resolution of Quantitative Phase Microscopy through Second-Harmonic Generation and Structured Illumination. In Proceedings of the TENCON 2022–2022 IEEE Region 10 Conference (TENCON), Hong Kong, China, 1–4 November 2022; pp. 1–3.
5. Gibson, G.; Courtial, J.; Padgett, M.J.; Vasnetsov, M.; Pas'ko, V.; Barnett, S.M.; Franke-Arnold, S. Free-space information transfer using light beams carrying orbital angular momentum. *Opt. Express* **2019**, *12*, 5448–5456. [CrossRef]
6. Li, S.; Bao, J.; Deng, Q.; Chen, L.;Wang, H. Frequency Conversion Interface towards Quantum Network: From Atomic Transition Line to Fiber Optical Communication Band. *Appl. Sci.* **2022**, *12*, 6522. [CrossRef]
7. Hong, X.H.; Yang, B.; Zhang, C.; Qin, Y.Q.; Zhu,Y.Y. Nonlinear volume holography for wave-front engineering. *Phys. Rev. Lett.* **2014**, *113*, 163902. [CrossRef]
8. Bowman, P.M.; Bowman, R. Tweezers with a twist. *Nat. Photonics* **2003**, *5*, 343–348.
9. Grier, D.G. A revolution in optical manipulation. *Nature* **2003**, *424*, 810–816. [CrossRef]
10. Pryamikov, A.; Hadzievski, L.; Fedoruk, M.; Turitsyn, S.; Aceves, A. Optical vortices in waveguides with discrete and continuous rotational symmetry. *J. Eur. Opt. Soc.-Rapid Public* **2021**, *17*, 23. [CrossRef]
11. Adcock, J.C.; Ding, Y. Quantum prospects for hybrid thin-film lithium niobate on silicon photonics. *Front. Optoelectron.***2022**, *15*, 7. [CrossRef]
12. Vinogradova, I.L.; Gizatulin, A.R.; Meshkov, I.K.; Bagmanov, V.K. Nonlinear materials for preparation of entangled states of light. In Proceedings of the Optical Technologies for Telecommunications 2021, Samara, Russian, 23–26 November 2021; p. 122950I.
13. Powers, P.E.; Haus, J.W. Chapter 5: Quasi-phase matching. In *Fundamental of Nonlinear Optics*; Liu, H., Ed.; CRC Press: Beijing, China, 2020; pp. 161–181.
14. Armstrong, J.A.; Bloembergen, N.; Ducuing, J.; Pershan, P.S. Interactions between light waves in a nonlinear dielectric. *Phys. Rev.* **1962**, *127*, 1918. [CrossRef]
15. Franken, P.A.; Hill, A.E.; Peters, C.W.; Weinreich, G. Generation of optical harmonics. *Phys. Rev. Lett.* **1961**, *7*, 118. [CrossRef]
16. Franken, P.A.; Ward, J.F. Optical harmonic and nonlinear phenomena. *Rev. Mod. Phys.* **1963**, *35*, 23. [CrossRef]
17. Fejer, M.M.; Magel, G.A.; Jundt, D.H.; Byer, R.L. Quasi-phase-matched second harmonic generation: Tuning and tolerances. *IEEE J. Quantum Elect.* **1992**, *28*, 2631–2654. [CrossRef]
18. Xue, Y.H.; Ming, N.B.; Zhu, J.S.; Feng, D. The second harmonic generation in $LiNbO_3$ crystals with period laminar ferroelectric domains. *Chin. Phys.* **1984**, *4*, 554–564.
19. Feisst, A.; Koidl, P. Current induced periodic ferroelectric domain structures in $LiNbO_3$ applied for efficient nonlinear optical frequency mixing. *Appl. Phys. Lett.* **1985**, *47*, 1125–1127. [CrossRef]
20. Wang, W.S.; Zhou, Q.; Geng, Z.H.; Feng, D. Study of $LiTaO_3$ crystals grown with a modulated structure I. second harmonic generation in $LiTaO_3$ crystals grown with period laminar ferroelectric domains. *J. Cryst. Growth* **1986**, *79*, 706–709.

21. Shur, V.Y.; Akhmatkhanov, A.R.; Baturin, I.S. Micro- and nano-domain engineering in lithium niobate. *Appl. Phys. Rev.* **2015**, *2*, 040604. [CrossRef]
22. Wang, T.; Chen, P.; Xu, C.; Zhang, Y.; Wei, D.; Hu, X.; Zhao, G.; Xiao, M.; Zhu, S. Periodically poled $LiNbO_3$ crystals from 1D and 2D to 3D. *Sci. China Technol. Sci.* **2020**, *63*, 1110–1126. [CrossRef]
23. Zhang, B.; Li, L.; Lu, Q.; Wang, L.; Chen, F. Frequency doubling in PPLN depressed-cladding waveguides written by femtosecond laser. *Opt. Mater.* **2022**, *125*, 112074. [CrossRef]
24. Lu, Y.L.; Lu, Y.Q.; Xue, C.C.; Ming, N.B. Growth of Nd^{3+}-doped $LiNbO_3$ optical superlattice crystals and its potential applications in self-frequency doubling. *Appl. Phys. Lett.* **1996**, *68*, 1467–1469. [CrossRef]
25. Zheng, J.J.; Lu, Y.Q.; Luo, G.P.; Ma, J.; Lu, Y.L.; Ming, N.B.; He, J.L.; Xu, Z.Y. Visible dual-wavelength light generation in optical superlattice Er:$LiNbO_3$ through upconversion and quasi-phase-matched frequency doubling. *Appl. Phys. Lett.* **1998**, *72*, 1808–1810. [CrossRef]
26. Xu, T.X.; Lu, D.Z.; Yu, H.H.; Zhang, H.J.; Zhang, Y.; Wang, J.Y. A naturally grown three-dimensional nonlinear photonic crystal. *Appl. Phys. Lett.* **2016**, *108*, 051907. [CrossRef]
27. Rosenman, G.; Urenski, P.; Agronin, A.; Rosenwaks, Y.; Molotskii, M. Submicron ferroelectric domain structures tailored by high-voltage scanning probe microscopy. *Appl. Phys. Lett.* **2003**, *82*, 103–105. [CrossRef]
28. Yamada, M.; Kishima, K. Fabrication of periodically reversed domain structure for SHG in $LiNbO_3$ by direct electron beam lithography beam lithography at room teperature. *Electron. Lett.* **1991**, *27*, 828–829. [CrossRef]
29. Hsu, W.; Gupta, M.C. Domain inversion in $LiTaO_3$ by electron beam. *Appl. Phys. Lett.* **1992**, *60*, 1–3. [CrossRef]
30. Muir, A.C.; Sones, C.L.; Mailis, S.; Eason, R.W.; Jungk, T.; Hoffmann, Á.; Soergel, E. Direct-writing of inverted domains in lithium niobate using a continuous wave ultra violet laser. *Opt. Express* **2008**, *16*, 2336–2350. [CrossRef]
31. Boes, A.; Steigerwald, H.; Crasto, T.; Wade, S.A.; Limboeck, T.; Soergel, E.; Mitchell, A. Tailor-made domain structures on the *x*- and *y*-face of lithium niobate crystals. *Appl. Phys. B* **2014**, *115*, 577–581. [CrossRef]
32. Berger, V. Nonlinear photonic crystals. *Phys. Rev. Lett.* **1998**, *81*, 4136. [CrossRef]
33. John, S. Strong localization of photons in certain disordered dielectric superlattices. *Phys. Rev. Lett.* **1987**, *58*, 2486–2489. [CrossRef]
34. Yablonovitch, E. Inhibited spontaneous emission in solid-state physics and electronics. *Phys. Rev. Lett.* **1987**, *58*, 2059–2062. [CrossRef]
35. Saltiel, S.M.; Neshev, D.N.; Fischer, R.; Krolikowski, W.; Arie, A.; Kivshar, Y.S. Generation of second-harmonic conical waves via nonlinear bragg diffraction. *Phys. Rev. Lett.* **2008**, *100*, 103902. [CrossRef]
36. Saltiel, S.M.; Neshev, D.N.; Krolikowski, W.; Arie, A.; Bang, O.; Kivshar, Y.S. Multiorder nonlinear diffraction in frequency doubling processes. *Opt. Lett.* **2009**, *34*, 848–850. [CrossRef]
37. Sheng, Y.; Kong, Q.; Roppo, V.; Kalinowski, K.; Wang, Q.; Cojocaru, C.; Krolikowski, W. Theoretical study of Čerenkov type second-harmonic generation in periodically poled ferroelectric crystals. *J. Opt. Soc. Am. B* **2012**, *29*, 312–318. [CrossRef]
38. Vyunishev, A.M.; Arkhipkin, V.G.; Chirkin, A.S. Frequency doubling of femtosecond laser pulses in three dimensional nonlinear photonic crystals. *Laser Phys. Lett.* **2023**, *20*, 035402 [CrossRef]
39. Trajtenberg-Mills, S.; Juwiler, I.; Arie, A. On-axis shaping of second-harmonic beams. *Laser Photonics Rev.* **2015**, *9*, L40–L44. [CrossRef]
40. Wang, C.; Chen, P.; Wei, D.; Zhang, L.; Zhang, Z.; Xu, L.; Hu, Y.; Li, J.; Zhang, Y.; Xiao, M.; et al. Sequential Three-Dimensional Nonlinear Photonic Structures for Efficient and Switchable Nonlinear Beam Shaping. *ACS Photonics* **2023**, *10*, 456–463. [CrossRef]
41. Wu, D.; Zhang, Z.; Wang, C.; Zhang, L.; Xu, L.; Wei, D.; Xiong, W.; Li, J.; Hu, Y.; Chu, J.; et al. Generation of nonlinear Airy beams withswitchable acceleration direction. *J. Opt.* **2023**, *25*, 07LT01. [CrossRef]
42. Jin, H.; Xu, P.; Luo, X.W.; Leng, H.Y.; Gong, Y.X.; Yu, W.J.; Zhong, M.L.; Zhao, G.; Zhu, S.N. Compact engineering of path-entangled sources from a monolithic quadratic nonlinear photonic crystal. *Phys. Rev. Lett.* **2013**, *111*, 023603. [CrossRef]
43. Trajtenberg-Mills, S.; Karnieli, A.; Voloch-Bloch, N.; Megidish, E.; Eisenberg, H.S.; Arie, A. Simulating correlations of structured spontaneously down-converted photon pairs. *Laser Photonics Rev.* **2020**, *14*, 1900321. [CrossRef]
44. Wang, A.D.; Zhu, L.; Chen, S.; Du, C.; Mo, Q.; Wang, J. Characterization of LDPC-coded orbital angular momentum modes transmission and multiplexing over a 50-km fiber. *Opt. Express* **2016**, *24*, 11716–11726. [CrossRef]
45. Yamada, M.; Nada, N.; Saitoh, M.; Watanabe, K. First order quasi-phase matched $LiNbO_3$ waveguide periodically poled by applying an external field for efficient blue second harmonic generation. *Appl. Phys. Lett.* **1993**, *62*, 435–436. [CrossRef]
46. Broderick, N.G.R.; Ross, G.W.; Offerhaus, H.L.; Richardson, D.J.; Hanna, D.C. Hexagonally poled lithium niobate: A two-dimensional nonlinear photonic crystal. *Phys. Rev. Lett.* **2000**, *84*, 4345–4348. [CrossRef]
47. Mizuuchi, K.; Morikawa, A.; Sugita, T.; Yamamoto, K. Electric-field poling in Mg-doped $LiNbO_3$. *J. Appl. Phys.* **2004**, *96*, 6585–6590. [CrossRef]
48. Zhang, B.; Wang, L.; Chen, F. Recent advances in femtosecond laser processing of $LiNbO_3$ crystals fir photonics applications. *Laser Photonics Rev.* **2000**, *14*, 1900407. [CrossRef]
49. Lin, J.T.; Bo, F.; Cheng, Y.; Xu, J.J. Advances in on-chip photonic devices based on lithium niobate on insulator. *Photonics Res.* **2020**, *8*, 1910–1936. [CrossRef]
50. Stoian, R.; Amico, C.D.; Bhuyan, M.K.; Cheng, G. [INVITED] Ultrafast laser photoinscription of large-mode-area waveguiding structures in bulk dielectrics. *Opt. Laser Technol.* **2016**, *80*, 98–103. [CrossRef]

51. Stuart, B.C.; Feit, M.D.; Herman, S.; Rubenchik, A.M.; Shore, B.W.; Perry, M.D. Nanosecond-to-femtosecond laser-induced breakdown in dielectrics. *Phys. Rev. B* **1996**, *53*, 1749. [CrossRef]
52. Qiu, J.; Miura, K.; Hirao, K. Three-dimensional optical memory using glasses as a recording medium through a multi-photon absorption process. *Jpn. J. Appl. Phys.* **1998**, *37*, 2263. [CrossRef]
53. Chan, J.W.; Huser, T.; Risbud, S.; Krol, D.M. Structural changes in fused silica after exposure to focused femtosecond laser pulses. *Opt. Lett.* **2001**, *26*, 1726–1728. [CrossRef]
54. Gorelik, T.; Will, M.; Nolte, S.; Tuennermann, A.; Glatzel, U. Transmission Electron Microscopy Studies of Femtosecond Laser Induced Modifications in Quartz. *Appl. Phys. A* **2003**, *76*, 309–311. [CrossRef]
55. Couairon, A.; Sudrie, L.; Franco, M.; Prade, B.; Mysyrowicz, A. Filamentation and damage in fused silica induced by tightly focused femtosecond laser pulse. *Phys. Rev. B* **2005**, *71*, 125435. [CrossRef]
56. Reichman, W.J.; Chan, J.W.; Smelser, S.W.; Mihailov, S.J.; Krol, D.M. Spectroscopic characterization of different femtosecond laser modification regimes in fused silica. *J. Opt. Soc. Am. B* **2007**, *24*, 1627–1632. [CrossRef]
57. Little, D.J.; Ams, M.; Dekker, P.; Marshall, G.D.; Dawes, J.M.; Withford, M.J. Femtosecond laser modification of fused silica: The effect of writing polarization on Si-O ring structure. *Opt. Express* **2008**, *16*, 20029–20037. [CrossRef] [PubMed]
58. Liu, Y.; Shimizu, M.; Zhu, B.; Dai, Y.; Qian, B.; Qiu, J.R.; Shimotsuma, Y.; Miura, K.; Hirao, K. Micromodification of element distribution in glass using femtosecond laser irradiation. *Opt. Lett.* **2009**, *34*, 136–138. [CrossRef] [PubMed]
59. Mishchik, K.; Cheng, G.; Huo, G.; Burakov, I.M.; Mauclair, C.; Mermillod-Blondin, A.; Rosenfeld, A.; Ouerdane, Y.; Boukenter, A.; Parriaux, O.; et al. Nanosize structural modifications with polarization functions in ultrafast laser irradiated bulk fused silica. *Opt. Express* **2010**, *18*, 24809–24824. [CrossRef] [PubMed]
60. Lancry, M.; Poumellec, B.; Chahid-Erraji, A.; Beresna, M.; Kazansky, P.G. Dependence of the femtosecond laser refractive index change thresholds on the chemical composition of doped-silica glasses. *Opt. Mater. Express* **2011**, *1*, 711–723. [CrossRef]
61. Toney Fernandez, T.; Haro-González, P.; Sotillo, B.; Hernandez, M.; Jaque, D.; Fernandez, P.; Domingo, C.; Siegel, J.; Solis, J. Ion migration assisted inscription of high refractive index contrast waveguides by femtosecond laser pulses in phosphate glass. *Opt. Lett.* **2013**, *38*, 5248–5251. [CrossRef]
62. Stuart, B.C.; Feit, M.D.; Rubenchik, A.M.; Shore, B.W.; Perry, M.D. Laser-Induced Damage in Dielectrics with Nanosecond to Subsecond Pulses. *Phys. Rev. Lett.* **1995**, *74*, 2248–2251. [CrossRef]
63. Yamada, K.; Watanabe, W.; Toma, T.; Itoh, K. In situ observation of photoinduced refractive-index changes in filaments formed in glasses by femtosecond laser pulses. *Opt. Lett.* **2001**, *26*, 19–21. [CrossRef]
64. Ponader, C.W.; Schroeder, J.F.; Streltsov, A.M. Origin of the refractive-index increase in laser-written waveguides in glasses. *J. Appl. Phys.* **2008**, *103*, 063516. [CrossRef]
65. Glezer, E.N.; Milosavljevic, M.; Huang, L.; Finlay, R.J.; Her, T.-H.; Callan, J.P.; Mazur, E. Three-Dimensional Optical Storage Inside Transparent Materials. *Opt. Lett.* **1996**, *21*, 2023–2025. [CrossRef] [PubMed]
66. Eberlea, G.; Schmidtb, M.; Pudec, F.; Wegenera, K. Laser surface subsurface of sapphireusing femtosecond pulses. *Appl. Surface Sci.* **2016**, *378*, 504–512. [CrossRef]
67. Kroesen, S.; Horn, W.; Imbrock, J.; Denz, C. Electro-optical tunable waveguide embeded multiscan Bragg grattings in Lithium niobate by direct femtosecond laser writting. *Opt. Express* **2014**, *22*, 23339–23348. [CrossRef]
68. Dai, Z.; Su, Q.; Wang, Y.; Qi, P.; Wang, X.; Liu, W. Fast fabrication of THz devices by femtosecond laser direct writing with a galvanometer scanner. *Laser Phys.* **2019**, *29*, 065301. [CrossRef]
69. Shivakumar, V.B.; Jedrkiewicz, O.; Hadden, J.P.; Sotillo, B.; Vázquez, M.R.; Dentella, P.; Fernandez, T.T.; Chiappini, A.; Giakoumaki, A.N.; Phu, T.L.; et al. Femtosecond laser written photonic and microfluidic circuits in diamond. *J. Phys. Photonics* **2019**, *1*, 022001.
70. Davis, K.M.; Miura, K.; Sugimoto, N.; Hirao, K. Writing waveguides in glass with a femtosecond laser. *Opt. Lett.* **1996**, *21*, 1729–1731. [CrossRef] [PubMed]
71. Miura, K.; Qiu, J.R.; Inouye, H.; Mitsuyu, T. Photowritten optical waveguides in various glasses with ultrashort pulse laser. *Appl. Phys. Lett.* **1997**, *71*, 3329–3331. [CrossRef]
72. Burghoff, J.; Grebing, C.; Nolte, S.; Tünnermann, A. Waveguides in lithium niobate fabricated by focused ultrashort laser pulses. *Appl. Surface Sci.* **2007**, *253*, 7899–7902. [CrossRef]
73. Burghoff, J.; Nolte, S.; Tünnermann, A. Origins of waveguiding in femtosecond laser-structured $LiNbO_3$. *Appl. Phys. A* **2007**, *89*, 127–132. [CrossRef]
74. Campbell, S.; Thomson, R.R.; Hand, D.P.; Kar, A.K.; Reid, D.T.; Canalias, C.; Pasiskevicius, V.; Laurell, F. Frequency-doubling in femtosecond laser inscribed periodically-poled potassium titanyl phosphate waveguides. *Opt. Express* **2007**, *15*, 17146–17150. [CrossRef] [PubMed]
75. Jia, Y.C.; Vázquez de Aldana, J.R.; Lu, Q.M.; Jaque, D.; Chen, F. Second harmonic generation of violet light in femtosecond-laser-inscribed BiB_3O_6 cladding waveguides. *Opt. Mater. Express* **2013**, *3*, 1279–1284. [CrossRef]
76. Hasse, K.; Calmano, T.; Deppe, B.; Liebald, C.; Kränkel, C. Efficient $Yb^{+3}CaGdAlO_4$ bulk and Femtosecond Laser-written Waveguide Lasers. *Opt. Lett.* **2015**, *40*, 3552–3555. [CrossRef] [PubMed]
77. Mishchik, K.; D'Amico, C.; Velpula, P.K.; Mauclair, C.; Boukenter, A.; Ouerdane, Y.; Stoiana, R. Ultrafast laser induced electronic and structural modifications in bulk fused silica. *J. Appl. Phys.* **2013**, *114*, 133502. [CrossRef]
78. Glezer, E.N.; Mazur, E. Ultrafast-laser driven micro-explosions in transparent materials. *Appl. Phys. Lett.* **1997**, *71*, 882–884. [CrossRef]

79. Thomas, J.; Hilbert, V.; Geiss, R.; Pertsch, T.; Tünnermann, A.; Nolte, S. Quasi phase matching in femtosecond pulse volume structured x-cut lithium niobate. *Laser Photonics Rev.* **2013**, *7*, L17–L20. [CrossRef]
80. Kroesen, S.; Tekce, K.; Imbrock, J.; Denz, C. Monolithic fabrication of quasi phase-matched waveguides by femtosecond laser structuring the $\chi^{(2)}$ nonlinearity. *Appl. Phys. Lett.* **2015**, *107*, 101109. [CrossRef]
81. Imbrock, J.; Wesemann, L.; Kroesen, S.; Ayoub, M.; Denz, C. Waveguide-integrated three-dimensional quasi-phase-matching structures. *Optica* **2020**, *7*, 28–34. [CrossRef]
82. Wei, D.; Wang, C.; Wang, H.; Hu, X.; Wei, D.; Fang, X.; Zhang, Y.; Wu, D.; Hu, Y.; Li, J.; et al. Experimental demonstration of a three-dimensional lithium niobate nonlinear photonic crystal. *Nat. Photonics* **2018**, *12*, 596–600. [CrossRef]
83. Wei, D.; Wang, C.; Xu, X.; Wang, H.; Hu, Y.; Chen, P.; Li, J.; Zhu, Y.; Xin, C.; Hu, X.; et al. Efficient nonlinear beam shaping in three-dimensional lithium niobate nonlinear photonic crystals. *Nat. Commun.* **2019**, *10*, 4193. [CrossRef]
84. Zhu, B.; Liu, H.G.; Chen, Y.P.; Chen, X.F. High conversion efficiency second-harmonic beam shaping via amplitude-type nonlinear photoniccrystals. *Opt. Lett.* **2019**, *45*, 220–223. [CrossRef]
85. Zhu, B.; Liu, H.G.; Liu, Y.A.; Yan, X.S.; Chen, Y.P.; Chen, X.F. Second-harmonic computer-generated holographic imaging through monolithic lithium niobate crystal by femtosecond laser micromachining. *Opt. Lett.* **2020**, *45*, 4132–4135. [CrossRef] [PubMed]
86. Shao, M.; Liang, F.; Yu, H.; Zhang, H. Pushing periodic-disorder induced phase matching into the deep-ultraviolet spectral region: theory and demonstration. *Light Sci. Appl.* **2020**, *9*, 45. [CrossRef] [PubMed]
87. Shao, M.; Liang, F.; Yu, H.; Zhang, H. Angular engineering strategy of an additional periodic phase for widely tunable phase-matched deep-ultraviolet second harmonic generation. *Light Sci. Appl.* **2022**, *11*, 2047–7538. [CrossRef]
88. Shao, M.; Liang, F.; Zhang, Z.; Yu, H.; Zhang, H. Spatial Frequency Manipulation of a Quartz Crystal for Phase-Matched Second-Harmonic Vacuum Ultraviolet Generation. *Laser Photonics Rev.* **2023**, 2300244. [CrossRef]
89. Yuan, T.; Zhu, B.; Tu, H.; Chen, Y.; Chen, X. Femtosecond laser direct writing quasi-phase matched type-II waveguide in lithium niobate. *Opt. Mater. Express* **2023**, *13*, 1–8. [CrossRef]
90. Fujimura, M.; Sohmura, T.; Suhara, T. Fabrication of domain-inverted gratings in MgO:$LiNbO_3$ by applying voltage under ultraviolet irradiation through photomask at room temperature. *Electron. Lett.* **2003**, *39*, 719–721. [CrossRef]
91. Muller, M.; Soergel, E.; Buse, K. Influence of ultraviolet illumination on the poling characteristics of lithium niobate crystals. *Appl. Phys. Lett.* **2003**, *83*, 1824–1826.
92. Dierolf, V.; Sandmann, C. Direct-write method for domain inversion patterns in $LiNbO_3$. *Appl. Phys. Lett.* **2004**, *84*, 3987-3989. [CrossRef]
93. Wengler, M.C.; Fassbender, B.; Soergel, E.; Buse, K. Impact of ultraviolet light on coercive field, poling dynamics and poling quality of various lithium niobate crystals from different sources. *J. Appl. Phys.* **2004**, *96*, 2816–2820. [CrossRef]
94. Sones, C.L.; Muir, A.C.; Ying, Y.J.; Mails, S.; Eason, R.W.; Jungk, T.; Hoffman, Á.; Soergel, E. Precision nanoscale domain engineering of lithium niobate via UV laser induced inhibition of poling. *Appl. Phys. Lett.* **2008**, *92*, 072905. [CrossRef]
95. Fujimura, M.; Suhara, T. Formation of MgO:LiNbO domain-inverted gratings by voltage application under UV light irradiation at room temperature. *Adv. Optoelectron.* **2008**, *2008*, 421054. [CrossRef]
96. Wang, W.J.; Kong, Y.F.; Liu, H.D.; Hu, Q.; Liu, S.G.; Chen, S.L.; Xu, J.J. Light-induced domain reversal in doped lithium niobate crystals. *J. Appl. Phys.* **2009**, *105*, 043105. [CrossRef]
97. Fujimura, M.; Kitado, E.; Inoue, T.; Suhara, T. MgO:$LiNbO_3$ waveguide quasi-phase-matched second-harmonic generation devices fabricated by two-step voltage application under UV light. *IEEE Photonics Tech. L.* **2011**, *23*, 1313–1315. [CrossRef]
98. Kitado, E.; Fujimura, M.; Suhara, T. Ultraviolet Laser Writing of Ferroelectric-Domain-Inverted Gratings for MgO:$LiNbO_3$ Waveguide Quasi-Phase-Matching Devices. *Appl. Phys. Express* **2013**, *6*, 102204. [CrossRef]
99. Boes, A.; Steigerwald, H.; Yudistira, D.; Sivan, V.; Wade, S.; Mailis, S.; Soergel, E.; Mitchell, A. Ultraviolet laser-induced poling inhibition produces bulk domains in MgO-doped lithium niobate crystals. *Appl. Phys. Lett.* **2014**, *105*, 092904. [CrossRef]
100. Fahy, S.; Merlin, R. Reversal of ferroelectric domains by ultrashort optical pulses. *Phys. Rev. Lett.* **1994**, *73*, 1122. [CrossRef] [PubMed]
101. Valdivia, C.E.; Sones, C.L.; Scott, J.G.; Mailis, S.; Eason, R.W.; Scrymgeour, D.A.; Gopalan, V.; Jungk, T.; Soergel, E.; Clark, I. Nanoscale surface domain formation on the $+z$ face of lithium niobate by pulsed ultraviolet laser illumination. *Appl. Phys. Lett.* **2005**, *86*, 022906. [CrossRef]
102. Zhu, H.S.; Chen, X.F.; Chen, H.G.; Deng, X.W. Formation of domain reversal by direct irradiation with femtosecond laser in lithium niobate. *Chin. Opt. Lett.* **2009**, *7*, 169–172.
103. Lao, H.Y.; Zhu, H.S.; Chen, X.F. Threshold fluence for domain reversal directly induced by femtosecond laser in lithium niobate. *Appl. Phys. A* **2010**, *101*, 313–317. [CrossRef]
104. Chen, X.; Karpinski, P.; Shvedov, V.; Koynov, K.; Wang, B.X.; Trull, J.; Cojocaru, C.; Krolikowski, W.; Sheng, Y. Ferroelectric domain engineering by focused infrared femtosecond pulses. *Appl. Phys. Lett.* **2015**, *107*, 141102. [CrossRef]
105. Chen, X.; Karpinski, P.; Shvedov, V.; Boes, A.; Mitchell, A.; Krolikowski, W.; Sheng, Y. Quasi-phase matching via femtosecond laser-induced domain inversion in lithium niobate waveguides. *Opt. Lett.* **2016**, *41*, 2410. [CrossRef]
106. Imbrock, J.; Hanafi, H.; Ayoub, M.; Denz, C. Local domain inversion in MgO-doped lithium niobate by pyroelectric field-assisted femtosecond laser lithography. *Appl. Phys. Lett.* **2018**, *113*, 252901. [CrossRef]
107. Xu, X.; Wang, T.; Chen, P.; Zhou, C.; Ma, J.; Wei, D.; Wang, H.; Niu, B.; Fang, X.; Wu, D.; et al. Femtosecond laser writing of lithium niobate ferroelectric nanodomains. *Nature* **2022**, *609*, 469–501. [CrossRef]

108. Wang, X.; Cao, Q.; Wang, R.-N.; Cao, X.; Liu, S. Manipulation of ferroelectric domain inversion and growth by optically induced 3D thermoelectric field in lithium niobate. *Appl. Phys. Lett.* **2022**, *121*, 181111. [CrossRef]
109. Maekawa, S.; Tohyama, T.; Barnes, S.E.; Ishihara, S.; Koshibae, W.; Khaliullin, G.; Appendices D. Thermoelectric Effects. In *Physics of Transition Metal Oxides*; Cardona, M., Ed.; Springer: Berlin/Heidelberg, Germany, 2004; pp. 323–331.
110. Kosorotov, V.F.; Kremenchugskij, L.S.; Levash, L.V.; Shchedrina, L.V. Tertiary pyroelectric effect in lithium niobate and lithium tantalate crystals. *Ferroelectrics* **1986**, *70*, 27–37. [CrossRef]
111. Bhatt, R.; Kar, S.; Bartwal, K.S.; Shula, V.; Sen, P.; Sen, P.K.; Wadhawan, V.K. Studies on nonlinear optical properties of ferroelectric MgO-LiNbO3 single crystals. *Ferroelectrics* **2005**, *323*, 165–169. [CrossRef]
112. Reddy, J.N.B.; Elizabeth, S.; Bhat, H.L.; Venkatram, N.; Rao, D.N. Influence of non-stoichiometric defects on nonlinear absorption and refraction in Nd:Zn co-doped lithium niobate. *Opt. Mater.* **2009**, *31*, 1022–1026. [CrossRef]
113. Xu, T.; Switkowski, K.; Chen, X.; Liu, S.; Koynov, K.; Yu, H.; Zhang, H.; Wang, Y.; Sheng, Y.; Krolikowski, W. Three-dimensional nonlinear photonic crystal in ferroelectric barium calcium titanate. *Nat. Photonics* **2018**, *12*, 591–595. [CrossRef]
114. Saltiel, S.M.; Neshev, D.N.; Krolikowski, W.; Voloch-Bloch, N.; Arie, A.; Bang, O.; Kivshar, Y.S. Nonlinear diffraction from a virtual beam. *Phys. Rev. Lett.* **2010**, *104*, 083902. [CrossRef]
115. Zhou, G.; Jesacher, A.; Booth, M.; Wilson, T.; Ródenas, A.; Jaque, D.; Gu, M. Axial birefringence induced focus splitting in lithium niobate. *Opt. Express* **2009**, *17*, 17970–17975. [CrossRef]
116. Karpinski, P.; Shvedov, V.; Krolikowski, W.; Hnatovsky, C. Laser-writing inside uniaxially birefringent crystals: Fine morphology of ultrashort pulseinduced changes in lithium niobate. *Opt. Express* **2016**, *24*, 7456–7476. [CrossRef]
117. Liu, S.; Switkowski, K.; Xu, C.; Tian, J.; Wang, B.; Lu, P.; Krolikowski, W.; Sheng, Y. Nonlinear wavefront shaping with optically induced three-dimensional nonlinear photonic crystals. *Nat. Commun.* **2019**, *10*, 3208. [CrossRef] [PubMed]
118. Liu, D.; Liu, S.; Mazur, L.M.; Wang, B.; Lu, P.; Krolikowski, W.; Sheng, Y. Smart optically induced nonlinear photonic crystals for frequency conversion and control. *Appl. Phys. Lett.* **2020**, *116*, 051104. [CrossRef]
119. Ostrovsky, A.S.; Rickenstorff-Parrao, C.; Arrizŏn, V. Generation of the perfect optical vortex using a liquid-crystal spatial light modulator. *Opt. Lett.* **2013**, *38*, 534–536. [CrossRef] [PubMed]
120. Topuzoski, S. Generation of optical vortices with curved fork-shaped holograms. *Opt. Quantum Electron.* **2016**, *48*, 138. [CrossRef]
121. Liu, S.; Mazur, L.M.; Krolikowski, W.; Sheng, Y. Nonlinear volume holography in 3D nonlinear photonic crystals. *Laser Photonics Rev.* **2020**, *14*, 2000224. [CrossRef]
122. Mazur, L.M.; Liu, S.; Chen, X.; Krolikowski, W.; Sheng, Y. Localized ferroelectric domains via laser poling in monodomain calcium barium niobate crystal. *Laser Photonics Rev.* **2021**, *15*, 2100088. [CrossRef]
123. Imbrock, J.; Szalek, D.; Laubrock, S.; Hanafi, H.; Denz, C. Thermally assisted fabrication of nonlinear photonic structures in lithium niobate with femtosecond laser pulses. *Opt. Express* **2022**, *30*, 39340–39352. [CrossRef]
124. Bhalla, A.S.; Newnham, R.E. Pyroelectric properties and phase transition in TRIS (dimethylammonium) nonabromodiantimonate uppercaseiii. *Solid State Commun.* **1988**, *67*, 1079–1083.
125. Cao, H.; Fang, B.; Xu, H.; Luo, H. Crystal orientation dependence of dielectric and piezoelectric properties of tetragonal $Pb(Mg_{1/3}Nb_{2/3})O_3$–38%$PbTiO_3$ single crystal. *Mater. Res. Bull.* **2002**, *37*, 2135–2143. [CrossRef]
126. Gopalan, V.; Mitchell, T.E.; Furukawa, Y.; Kitamura, K. The role of nonstoichiometry in 180° domain switching of $LiNbO_3$ crystals. *Appl. Phys. Lett.* **1998**, *72*, 1981–1983. [CrossRef]
127. Kim, S.; Gopalana, V.; Gruverman, A. Coercive fields in ferroelectrics: A case study in lithium niobate and lithium tantalate. *Appl. Phys. Lett.* **2002**, *80*, 2740–2742. [CrossRef]
128. Chen, X.; Liu, D.; Liu, S.; Mazur, L.M.; Liu, X.; Wei, X.; Xu, Z.; Wang, I.; Sheng, Y.; Wei, Z.; et al. Optical induction and erasure of ferroelectric domains in tetragonal PMN-38PT crystals. *Adv. Opt. Mater* **2021**, *10*, 2102115. [CrossRef]
129. Chen, X.; Mazur, L.M.; Liu, D.; Liu, S.; Liu, X.; Xu, Z.; Wei, X.; Wang, J.; Sheng, Y.; Wei, Z.; et al. Quasi-phase matched second harmonic generation in a PMN-38PT crystal. *Opt. Lett.* **2022**, *47*, 2056–2059. [CrossRef] [PubMed]
130. Zhang, Y.; Wen, J.; Zhu, S.N.; Xiao, M. Nonlinear talbot effect. *Phys. Rev. Lett.* **2012**, *104*, 183901. [CrossRef] [PubMed]